Eur. J. Mech. B/Fluids 18 (1999) 581–620

On the application of e^n-methods to three-dimensional boundary-layer flows

R.J. Lingwood

Department of Engineering, University of Cambridge, Trumpington Street, Cambridge CB2 1PZ, UK

(Received 15 July 1998; revised 25 November 1998; accepted 6 January 1999)

Abstract – Extension of the e^n-method from two-dimensional to three-dimensional boundary-layer flows has not been straightforward. Confusion has centred on whether to use temporal or spatial stability theories, conversion between the two approaches, and the choice of integration path. The aim of this study is to clarify the confusion about the direction and magnitude of maximum growth in convectively unstable three-dimensional non-parallel boundary layers. To this end, the time-asymptotic response of the boundary layer to an impulsive point excitation is considered. Since all frequencies and all wavenumbers are excited by an impulsive point source, the most amplified component of the response is equivalent to the result of maximizing the growth over arbitrary choices of harmonic point excitation; the standard e^n-approach. The impulse response is calculated using a spatial steepest-descent method, which is distinct from the earlier Cebeci–Stewartson method. It is necessary to allow both time and spanwise distance to become complex during integration, but with the constraint that both are real at the end point. This method has been applied to the two-dimensional Blasius boundary layer, for which validation of the method is more straightforward, and also to a three-dimensional Falkner–Skan–Cooke (with non-zero pressure gradient and sweep) boundary layer. Dimensional frequencies and spanwise wavenumbers of propagating components are kept constant (although not necessarily real), as is physically relevant to steady flows with spatial inhomogeneity in the chordwise direction only. With this method a spatial approach is taken without having to make a priori choices about the value of disturbance frequency or wavenumber. Further, purely by choosing a downstream observation point, it is possible to find the maximum-amplitude component directly without having to calculate the entire impulse response (or wave packet). If the flow is susceptible to more than one convective instability mode, provided the modes are separated in the frequency–wavenumber space, separate n-factors can be calculated for each mode. Wave-packet propagation in the Ekman layer (a strictly parallel three-dimensional boundary layer) is also discussed to draw comparisons between the conditions for maximum growth in parallel and non-parallel boundary layers. © Elsevier, Paris

1. Introduction

The prediction of laminar–turbulent transition in boundary-layer flows is of great importance. Currently, the most popular method for transition prediction is the e^n-method, which is based on linear stability only; receptivity, bypass mechanisms and nonlinear mechanisms are neglected. The principle of the e^n-method in two-dimensional boundary layers is discussed fully by Arnal [1]. A local stability analysis is applied over a range of downstream positions. Assuming for now that the boundary layer is non-parallel (and not absolutely unstable), waves of certain fixed real frequencies will become amplified at some downstream location and then become damped again farther downstream. The principle of the e^n-method is to relate the downstream growth of waves to their amplitude at the neutral point. Since receptivity mechanisms are neglected in the e^n-method, the true initial amplitude of a wave is unknown but it has been observed experimentally (Smith and Gamberoni [2], van Ingen [3]) that in two-dimensional boundary layers the natural logarithm of the ratio of the wave amplitude at the transition point compared with the amplitude at the neutral point of the wave that undergoes the largest growth within the unstable region is between seven and ten. For example, from a spatial viewpoint, where the wavenumber α of a disturbance is complex (henceforth the subscripts r and i are used to denote real and imaginary parts, respectively) and the frequency is real, the growth of a wave of fixed frequency is characterized by

$$\ln\left(\frac{A}{A_0}\right) = -\int_{x_0}^{x} \alpha_i \, dx, \tag{1}$$

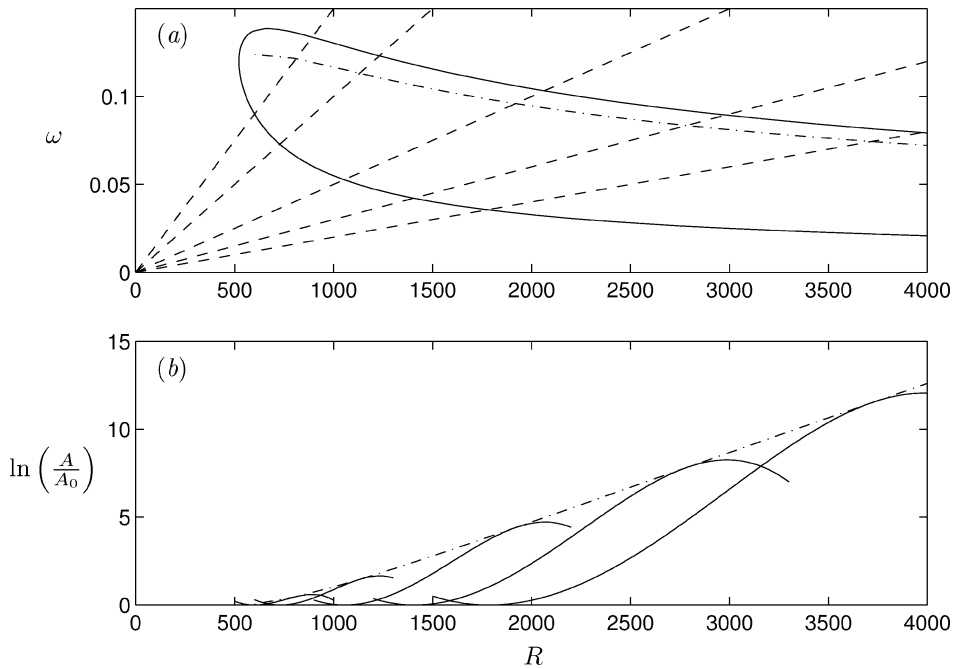

Figure 1. (a) The neutral-stability curve for the Blasius boundary layer (——), lines of constant dimensional frequency (– – –) and the locus of points defining the n-curve (— · — ·). (b) Amplitude curves for a selection of constant dimensional frequencies and the envelope defining the n-curve (— · — ·).

where A denotes the disturbance amplitude, the subscript 0 denotes the neutral point, and x is the downstream coordinate. The spatial n-factor is this quantity maximized over all frequencies. *Figure 1* illustrates the method for the Blasius boundary-layer flow. *Figure 1(a)* shows the neutral-stability curve in the (ω, R)-plane (where R is the Reynolds number and ω is the non-dimensional frequency, such that ω/R is proportional to the dimensional frequency) and the dashed lines have constant gradient and represent paths of constant dimensional frequency through the unstable region inside the neutral-stability curve. In *figure 1(b)*, the amplitude ratio given by (1) is plotted for the fixed frequencies pictured in *figure 1(a)*. Clearly, the waves begin to grow as they enter the unstable region, i.e. cross the lower branch of the neutral-stability curve, and begin to decay as they cross the upper branch. The low frequencies begin to grow farther downstream than the high frequencies, and they achieve larger amplitudes. The dashed-dotted line in *figure 1(b)* is an envelope curve for all the amplitude-ratio curves, such that it is tangential to the maximum amplitude ratio of any frequency wave at all R, i.e. it is the n-factor. The dashed-dotted in *figure 1(a)* is a projection of the n-factor on to the (ω, R)-plane, where it lies close to the upper branch. The e^n-method has also been applied using temporal stability theory, giving rise to the following expression in which Gaster's transformation (Gaster [4], which is valid close to the neutral-stability curve only) is used to convert the temporal growth rates to spatial ones:

$$\ln\left(\frac{A}{A_0}\right) = \int_{x_0}^{x} \frac{\omega_i}{V_g}\, dx, \tag{2}$$

where $V_g = \partial\omega_r/\partial\alpha_r$. The temporal n-factor is given by (2) maximized over all frequencies and usually agrees quite closely with the spatial n-factor.

Three-dimensionality of the boundary layer introduces an extra wavenumber (or, equivalently, a wave angle) and also introduces the possibility of several coexisting modes of instability. Because of the extra degree of freedom, temporal theory (having complex ω but real wavenumbers α and β) is attractive for tackling three-

dimensional boundary layers; spatial theory has real ω but both α and β are complex. Extension of the e^n-method to three-dimensional boundary-layer flows has taken a number of routes, leaving confusion about which direction to integrate the growth of disturbances, confusion about the appropriateness of temporal versus spatial stability theories, and about how to convert the magnitude and direction of temporal results into spatial ones when the group velocity vector is complex. Section 3 of Arnal [1], and the references therein, demonstrate the complexity of existing methods developed to tackle three-dimensional e^n-calculations. When temporal stability theory is used, a generalized form of Gaster's transformation is used. Temporal growth rates ω_i are converted to spatial ones using the norm of the group velocity vector, which has components $\partial\omega/\partial\alpha$ and $\partial\omega/\partial\beta$ (both of which are in general complex, although the imaginary parts are unsatisfactorily assumed to be small and are neglected). Integration is performed along a path defined by the direction of the group velocity vector (again requiring that the imaginary part of the group velocity is neglected), which is often approximated by the potential flow direction. If spatial theory is used, there are too many unknowns and a decision about one parameter (usually the imaginary part of the secondary wavenumber β_i) must be made. In a study of infinite swept wings, Mack [5] proposed that $\beta_i = 0$, i.e. that only growth of disturbances in the x-direction be considered. The simplicity of this suggestion is attractive, but is of questionable validity. Alternatively, Cebecis and Stewartson [6] suggested using the saddle-point (or steepest-descent) method for waves of fixed real frequency, in which the large-x solution for fixed y/x (where y is perpendicular to x and in the plane of the boundary) imposes the condition that $\partial\alpha/\partial\beta$ is purely real. This saddle-point condition holds for specific combinations of α and β, which in general are both complex, and thus β_i is calculated at successive x-positions. One problem with this method is that the saddle-point condition relevant to parallel flows is applied to non-parallel flows, which can only be valid in a restricted region of the (x, y)-plane. Further, for flows of infinite extent in the y-direction (or periodic in y, as discussed by Cebeci and Stewartson [6]) the physical value of β should be constant (although not necessarily real). Nayfeh [7] also discussed the use of the saddle-point method for monochromatic waves and wave packets in parallel and non-parallel three-dimensional boundary layers. His conclusions for *parallel* flows are consistent with those of Cebeci and Stewartson [6]; for *non-parallel* flows Nayfeh gives a modified form of the parallel-flow saddle-point conditions. It is shown here that Nayfeh's non-parallel saddle-point method should be modified in order to represent the physical propagation of wave packets and, furthermore, that it is not necessary to calculate the whole wave-packet response in order to find the maximum-amplitude component; by appropriate choices of ω and β, the maximum-amplitude component can be calculated directly.

The methods mentioned above based on the propagation of monochromatic waves require that growth rates are repeatedly calculated according to the chosen criterion (often a decision that seems to be based on intuition rather than any rigorous argument) and then maximized following a second rule of which again there are several possible choices (Arnal [1]): the envelope method (for each frequency the wave angle is optimized to obtain the maximum growth rate at each downstream position, which are then integrated between the chosen start and end points, and the integrated growths are then maximized over all ω), or the numerous envelope-of-envelopes methods (maximized over ω and β, or over ω and the wavelength, or over ω and the wave angle). The existence of more than one instability mode, e.g. crossflow instability (which is inviscid in nature and dominates at large Reynolds numbers) and a viscous instability mode that dominates at lower Reynolds numbers, is common in three-dimensional boundary layers. This fact further complicates the maximization procedure because depending on which maximization method has been chosen, i.e. what is held constant as the growth rates are integrated along the chosen path, abrupt changes can occur as the dominance of the coexisting instability modes changes. For example, the envelope method, which seems to be the most popular choice, makes no distinction between different instability mechanisms. Nor does the envelope method track the growth of a physical wave, but pieces together different waves that have the maximum growth rate at successive downstream positions, irrespective of the relative amplitudes that those different waves have gained due to their

differing growth rates at more upstream positions. In general, different methods give different results, which is clearly unsatisfactory.

The aim of this paper is not to predict the value of the n-factor required for transition, which requires comparison with experimental data, nor to discuss the general shortcomings of the e^n-method, but is to clarify the confusion about the direction and magnitude of maximum growth of the spectrum of normal modes in three-dimensional boundary layers. To this end, the response of the boundary layer to an impulsive point excitation is considered. There may be a concern that this response would not provide useful information if the boundary layer were excited by a causal, but then continuous, harmonic excitation rather than the transient excitation. For an arbitrary frequency of harmonic excitation, the impulse response will give results applicable to the transient response due to the switching-on of the excitation, but the long-time response will be determined by the dispersion characteristics of the chosen frequency. However, if the boundary layer is excited at the most unstable frequency, the most amplified component of the transient and the long-time response follow the same path. Thus, since standard e^n-methods involve taking all arbitrary choices of harmonic excitation and maximizing to find the most unstable frequency, it is enough to calculate the impulse response (i.e. the response to excitation over all frequencies simultaneously) and determine the positions and magnitudes of maximum-amplitude components from that.

The concept of e^n-calculations relies on there being no absolute instability, which is characterized by disturbances growing in time at fixed locations and, therefore, to disturbance amplitudes that inevitably reach levels where nonlinearity cannot be neglected. If there is no absolute instability, then (using the terminology of Huerre and Monkewitz [8]) we can safely think of the boundary layer as a spatial *amplifier* of input disturbances with real frequency if required; otherwise, the boundary layer behaves as an *oscillator* and a purely spatial approach (real frequency) to the problem is not valid. For the most part, only maxima of wave packets are calculated in this paper and, in general, maxima are convective even if the flow is absolutely unstable, i.e. maxima travel along rays of non-zero x/t (and y/t in three-dimensional boundary layers) even if along a ray of zero x/t (and y/t) there is temporal growth indicating absolute instability; see figure 1 of Lingwood [9]. Thus, unless an initial Briggs' analysis (Briggs [10], Bers [11]) has been performed to establish the absolute or convective nature of the flow in question at all relevant Reynolds number, simply calculating maximum growth rates (although still valid) would miss an absolute instability of a component of the impulse response, or wave packet, that does not give the maximum. As yet, no three-dimensional boundary-layer flow has been shown to be truly absolutely unstable. However, recent studies of certain three-dimensional boundary layers (Lingwood [9,12–15]) have shown unidirectional absolute instability, i.e. growth in time at fixed x-positions, say, but with continued convective growth in the y-direction. It is suggested in these papers that this phenomenon may be particularly important in cylindrical-polar systems (x becomes the radial direction and y becomes the azimuthal direction), where the onset of absolute instability implies that disturbances are constrained to convect around circular paths as they grow in time, leading to increasing amplitudes at fixed radial positions and possibly triggering the onset of transition. No cylindrical-polar systems are considered in this paper but, of the three boundary-layer flows considered, two do have unidirectional absolute instability in certain regimes. The first is the linear Ekman layer (Lingwood [13]) and secondly the Falkner–Skan–Cooke (FSC) boundary layer (Lingwood [16]). However, the particular FSC boundary layer studied here does not exhibit absolute instability, at least at relevant Reynolds numbers. That leaves the Ekman layer, for which it should be borne in mind that the unidirectional absolute instability above a critical Reynolds number may have implications for the location of the start of nonlinear behaviour.

Here, the impulse response is calculated using the steepest-descent method, which (in most part due to the seminal contributions by Gaster) is now an established technique for analysis of boundary layers. The linear Ekman layer is strictly parallel and for this reason is used in Section 2 to illustrate the steepest-

descent method applied to the simplest form of three-dimensional boundary layer. The mean flow and the stability analysis are described in Sections 2.1 and 2.2, respectively. The steepest-descent method is described in Section 2.3, followed by a comparison with existing methods applied to parallel boundary layers; see Section 2.4. A numerical-integration scheme (outlined in Section 2.5) is also used to solve for the impulse response. The results from the steepest-descent method are compared with the solution based on numerical integration in Section 2.6. Concluding comments on the analysis of the Ekman layer are given in Section 2.7, where it is shown that, although the maximum-amplitude component in parallel flows can be determined very easily, piecing together maximum growth rate components from successive parallel flows with varying Reynolds number would not give the growth relevant to any physical wave. Non-parallel boundary layers are discussed in Section 3. First, in Section 3.1, the Blasius boundary layer is used to illustrate the steepest-descent method applied to a non-parallel two-dimensional boundary layer, for which validation of the method is easier. Following some comments in Section 3.2, the method is applied to a three-dimensional non-parallel FSC boundary layer with constant (non-zero) sweep and pressure gradient; see Section 3.3. For non-parallel boundary layers it is necessary to allow time and (in the three-dimensional case) spanwise distance to be complex with the constraint that both are real at the end point. This FSC boundary layer is not intended to realistically model a swept-wing boundary layer but is used to illustrate the method, which could easily be applied to a more complicated basic flow generated by a boundary-layer code. Comparison with existing three-dimensional e^n-methods is given in Section 3.4, followed by some concluding remarks in Section 4.

2. Parallel three-dimensional flows—the Ekman layer

2.1. The mean flow

Ekman [17] analysed the problem of a wind-driven rotating flow resulting from balanced pressure gradient, Coriolis and frictional forces. He showed that the flow has a boundary-layer structure. Approximate Ekman layers occur in the atmospheric boundary layer and in wind-driven surface layers of the ocean, but turbulence always plays a role in these. Here, only steady laminar mean flows are considered. The linear Ekman layer (in which nonlinear inertial terms are negligible in comparison with the Coriolis terms, i.e. the zero Rossby number limit) is an exact solution of the Navier–Stokes equations and is strictly parallel; it has constant boundary-layer thickness and is therefore parallel in the physical sense, and has a constant characteristic velocity giving a single Reynolds-number definition for the flow. Thus, it is not necessary to account for downstream growth of the boundary layer or to make a local parallel-flow approximation to reduce the governing partial differential equations to a more amenable ordinary differential set.

Ekman's analysis is applied to a large body of fluid at rest relative to a uniformly rotating rigid boundary. The fluid is set into motion by a uniform pressure gradient (modified to incorporate effects of gravity and centrifugal force), which is then balanced by the Coriolis force. If the pressure gradient lies in the (x^*, y^*)-plane, which rotates about the z^*-axis at Ω^* (asterisks will be used here to denote dimensional quantities), with components $(0, -P_y^*)$, then the equations giving the mean velocity components (U^*, V^*) in the Ekman layer near the boundary $(z^* = 0)$ are

$$-2\Omega^* V^* = \nu^* \frac{\partial^2 U^*}{\partial z^{*2}}, \tag{3}$$

$$2\Omega^* U^* = \frac{P_y^*}{\rho^*} + \nu^* \frac{\partial^2 V^*}{\partial z^{*2}}, \tag{4}$$

where ρ^* and ν^* are the fluid density and kinematic viscosity, respectively. There are no-slip boundary conditions at $z^* = 0$ and the velocity at large z^* is $U^*_\infty = P^*_y/(2\rho^*\Omega^*)$. The non-dimensionalized analytic solution to (3)–(4) is

$$U(z) = \frac{U^*}{U^*_\infty} = 1 - e^{-z}\cos z, \tag{5}$$

$$V(z) = \frac{V^*}{U^*_\infty} = e^{-z}\sin z, \tag{6}$$

where $z = z^*/l^*$ and $l^* = (\nu^*/\Omega^*)^{1/2}$. The mean velocity components are plotted in figure 1 of Lingwood [13].

2.2. The linear stability analysis

The non-dimensional Navier–Stokes equation, in a frame rotating at Ω^*, and continuity equation are

$$\frac{\partial \widetilde{\mathbf{U}}}{\partial t} + (\widetilde{\mathbf{U}}\cdot\boldsymbol{\nabla})\widetilde{\mathbf{U}} + \frac{2}{R}\mathbf{k}\times\widetilde{\mathbf{U}} = -\nabla\widetilde{P} + \frac{1}{R}\nabla^2\widetilde{\mathbf{U}}, \tag{7}$$

$$\boldsymbol{\nabla}\cdot\widetilde{\mathbf{U}} = 0. \tag{8}$$

Here, t is time, $\widetilde{\mathbf{U}} = [\widetilde{U}, \widetilde{V}, \widetilde{W}]^{\mathrm{T}}$ where the components of the vector are the instantaneous velocities each composed from a sum of the mean velocity and a small perturbation velocity, $\widetilde{P}$ is the instantaneous pressure, $R = U^*_\infty l^*/\nu^*$ is the Reynolds number, $\mathbf{k}$ is the unit vector in the z-direction and ∇^2 is the Laplacian operator. The non-dimensionalizing velocity, pressure and time scales are U^*_∞, $\rho^* U^{*2}_\infty$ and l^*/U^*_∞, respectively. Subtracting the mean flow from (7)–(8), linearizing with respect to the perturbation quantities and neglecting terms higher than $\mathrm{O}(R^{-2})$ results in equations that are separable in x, y and t (without any parallel-flow approximation) and perturbation quantities that can be expressed in normal-mode form

$$[u, v, w, p]^{\mathrm{T}} = \left[\hat{u}(z), \hat{v}(z), \hat{w}(z), \hat{p}(z)\right]^{\mathrm{T}} e^{i(\alpha x + \beta y - \omega t)}. \tag{9}$$

Here, for example, $\hat{u}$ is the spectral representation of the perturbation u, α and β are the wavenumbers in the x- and y-directions, respectively, ω is the disturbance frequency. The perturbation equations are given in Lingwood [13] and are equivalent to the Orr–Sommerfeld equation with additional terms due to Coriolis effects.

The solution of the governing equations subject to impulsive point forcing at x_0 and y_0 is considered, namely the vertical velocity at $z = 0$ is given by

$$w(0; x, y, t) = \delta(X)\delta(Y)\delta(t), \tag{10}$$

where δ is the Dirac delta function, $X = x - x_0$ and $Y = y - y_0$. The additional boundary conditions at $z = 0$, given by the no-slip condition, are

$$u(0; x, y, t) = v(0; x, y, t) = 0, \tag{11}$$

and as $z \to \infty$ all perturbations must decay. Solution of an inhomogeneous system such as this is described in detail in Lingwood [15]. The problem reduces to solving a Green's function of the form

$$w(z; x, y, t) = \frac{1}{(2\pi)^3}\int_B\int_A\int_W \frac{\Phi(z; \alpha, \beta, \omega; R)}{\Delta_0(\alpha, \beta, \omega; R)} e^{i(\alpha X + \beta Y - \omega t)}\, d\omega\, d\alpha\, d\beta, \tag{12}$$

where Φ is a function of z formed from a combination of the independent solution vectors of the governing ordinary differential equations, $\Delta_0 = 0$ is the dispersion relation, which is satisfied by the discrete eigenvalues of the homogeneous problem (the unforced case) and A, B and W are inversion contours in the α-, β- and ω-planes, respectively.

The inversion contours must lie in regions of analyticity in the respective complex planes. Therefore, the contours must avoid continuous and discrete singularities. If the inversion contours are incorrectly taken through regions of non-analyticity, the inversions can still be formally carried out but, as well as being non-causal, the solution may not converge to a solution of the original problem. In both the α- and β-planes there is a strip of analyticity of non-zero width, centred on the respective real axes. Taking the A- and B-contours along the real α- and β-axes, respectively, gives purely temporal branches of the dispersion relation in the ω-plane. The region of analyticity in the ω-plane lies above, and includes, the horizontal W-contour (sometimes referred to as the Bromwich contour) that must lie above all the discrete singularities and branch cuts given by the A- and B-contours for zero response at $t < 0$. The W-contour produces spatial (although not *purely* spatial since they have complex ω, with positive ω_i) branches of the dispersion relation in the α- and β-planes. With ω_i above any singularities in the ω-plane, the spatial branches do not cross the real α- and β-axes and they correspond to spatially damped eigenvalue solutions. It follows that any branch lying in the upper-half α-plane (β-plane) leads to a response in the physical region $X > 0$ ($Y > 0$), while any branch lying in the lower-half α-plane (β-plane) corresponds to the region $X < 0$ ($Y < 0$). The above choice of contours ensures convergence of the transforms and satisfies causality.

2.3. The method of steepest descent

The integrals given by (12) give the exact solution for the axial perturbation velocity w, when the boundary-layer flow is impulsively disturbed in the way described by (10). The solution can be evaluated by direct numerical integration or, alternatively, by asymptotic methods, in which only dominant terms are considered. Here, concepts from the method of steepest descent, in which X/t and Y/t are kept constant as $t \to \infty$, are used to predict the time-asymptotic approximations to the maximum growth rate and direction of maximum growth. These approximations will be compared with the solution of (12) calculated by numerical integration.

Neglecting the continuous spectra (the branch-cut contributions), the ω-integral is performed first by closing the W-contour with semi-circles at infinity and using the residue theorem

$$w(z; x, y, t) = \frac{H(t)}{(2\pi)^2 i} \int_B \int_A \sum_{j=1}^{M} \Theta_j(z; \alpha, \beta) e^{-i\psi_j(\alpha,\beta)t}\, d\alpha\, d\beta, \tag{13}$$

where

$$\Theta_j(z; \alpha, \beta) = \frac{\Phi(z; \alpha, \beta, \omega_j(\alpha, \beta); R)}{\partial \Delta_0(\alpha, \beta, \omega_j(\alpha, \beta); R)/\partial \omega_j} \tag{14}$$

and

$$\psi_j(\alpha, \beta) = -\left(\frac{\alpha X}{t} + \frac{\beta Y}{t} - \omega_j(\alpha, \beta)\right). \tag{15}$$

Here, ψ_j is the complex phase function, M is the number of discrete first-order poles $\omega_j(\alpha, \beta)$ of the ω-integrand and $H(t)$ is the unit-step function in time. In general, the function $\Theta_j(z; \alpha, \beta)$ has branch-pole singularities (due to poles coalescing) at branch points of $\omega(\alpha, \beta)$, where $\partial \Delta_0/\partial \omega = 0$ and $\partial \omega/\partial \alpha = \partial \omega/\partial \beta = \infty$. However, the sum over all j does not have any singularities; the summation $\sum_{j=1}^{M} \Theta_j(z; \alpha, \beta)$ is

an entire function. This must be so, because the branch points of $\omega(\alpha, \beta)$ are just multiple roots of ω for some α and β, all roots are included in the residue evaluation, and the terms that individually have a singularity cancel. (Coalescing residues do not cancel if they pinch the integration contour, but it is not possible for multiple roots of ω to pinch the W-contour because there are no discrete poles above the W-contour from causality arguments.)

The method of steepest descent is used to evaluate the large-time solution of the remaining α- and β-integrals along rays of constant X/t and Y/t. The best approximation to these integrals is given by choosing paths where large values of $\psi_{ji}(\alpha, \beta)$ are concentrated in as short a length as possible and where ψ_j is stationary. When $\partial^2\psi_j/\partial\alpha^2 \neq 0$, it is easy to show (using the Cauchy–Riemann equations) that all stationary points of ψ_j are saddle points. So, if the end points of each steepest-descent integration are separated by, say, a single saddle point of ψ_j, the A- and B-contours (along the real α- and β-axes, respectively) are deformed onto steepest-descent paths that pass through the saddle points $\alpha^\star$ and $\beta^\star$ (at which $\partial\psi_j/\partial\alpha = 0$ and $\partial\psi_j/\partial\beta = 0$, respectively), where $\omega_j^\star \equiv \omega_j(\alpha^\star, \beta^\star)$ and $\psi_j^\star \equiv \psi_j(\alpha^\star, \beta^\star)$. A steepest-descent path lies along a line where ψ_{ji} decreases most rapidly, namely orthogonal to the lines of constant ψ_{ji}, and is therefore (from the Cauchy–Riemann equations) given by a line of constant ψ_{jr} through the saddle point. In general, the limits of the integral do not lie on the steepest-descent path, but they can be joined to it within valleys of ψ_{ji}, i.e. within regions where $\psi_{ji} < \psi_{ji}^*$.

As $t \to \infty$, with fixed X/t and Y/t, integration along the steepest-descent paths is dominated by contributions from the saddle points of ψ_j, where $\partial\psi_j/\partial\alpha = \partial\psi_j/\partial\beta = 0$ and where ψ_j is given by (15). At these saddle points,

$$\left.\frac{\partial\omega_j}{\partial\alpha}\right|_{\alpha^\star,\beta^\star} = \frac{X}{t}, \qquad \left.\frac{\partial\omega_j}{\partial\beta}\right|_{\alpha^\star,\beta^\star} = \frac{Y}{t}, \tag{16}$$

which are real and therefore

$$\left.\frac{\partial\omega_{jr}}{\partial\alpha_r}\right|_{\alpha^\star,\beta^\star} = \frac{X}{t}, \qquad \left.\frac{\partial\omega_{ji}}{\partial\alpha_r}\right|_{\alpha^\star,\beta^\star} = 0, \tag{17}$$

and similarly for $(\partial\omega_j/\partial\beta)|_{\alpha^\star,\beta^\star}$. Assuming that there is a single saddle point of ψ_j through which the integration contour can be made to pass for each value of j, following standard mathematics text books, the time-asymptotic impulse response to (13) reduces to

$$w(z; x, y, t) \sim \frac{iH(t)}{2\pi}\sum_{j=1}^{M}\frac{\Theta_j(z; \alpha^\star, \beta^\star)e^{i(\alpha^\star X+\beta^\star Y-\omega_j^\star t)}}{f_j(\alpha^\star, \beta^\star)t}, \tag{18}$$

where

$$f_j(\alpha^\star, \beta^\star) = \left[\left(\frac{\partial^2\omega_j}{\partial\alpha\partial\beta}\right)^2 - \frac{\partial^2\omega_j}{\partial\alpha^2}\frac{\partial^2\omega_j}{\partial\beta^2}\right]^{1/2}\Bigg|_{\alpha^\star,\beta^\star}, \tag{19}$$

and where Θ_j/f_j is a function that gives the leading-order term of the asymptotic approximation. In practice, for the time-asymptotic response, the summation over M is limited to the number of unstable modes. The physical solution is given by the real part of (18). Note that, in general, it is not possible to deform an integration path through all saddle points; see Lingwood [15]. Therefore, it is not sufficient simply to locate saddle points of the complex phase function without examining the global topography of the phase function. However, further discussion of this point in Section 2.6 shows that the integration contour can always be deformed through the maximum-growth saddle point.

As X/t and Y/t vary, the respective saddle points trace paths in the complex α- and β-planes; each point being related to a ray in the physical (x, t)- and (y, t)-spaces. Along each ray the response is dominated by the exponential term of Eq. (18) and has the form of a travelling wave with constant complex values of frequency and streamwise and crossflow wavenumbers. The temporal growth rate along rays is

$$\psi_{ji}^{\star} = \omega_{ji}^{\star} - \frac{\alpha_i^{\star} X}{t} - \frac{\beta_i^{\star} Y}{t}. \tag{20}$$

Following the response along given rays corresponds to a moving observation position travelling at $(\partial\omega_j/\partial\alpha)|_{\alpha^\star,\beta^\star}$ and $(\partial\omega_j/\partial\beta)|_{\alpha^\star,\beta^\star}$ in the x- and y-directions, respectively. If $\psi_{ji}^{\star}$ is positive, the disturbance grows in time in that reference frame; if $\psi_{ji}^{\star}$ is negative, the waves decay in amplitude as they travel and the flow returns to its undisturbed state.

Temporal surfaces of the dispersion relation given by real values of α and β can be used to identify certain saddle points of ψ; see Gaster [18]. Maxima of the imaginary part of the temporal surfaces, i.e. $\omega_i(\alpha_r, \beta_r)$ (dropping the j subscript), satisfy the saddle-point conditions (16) because at these points $\partial\omega_i/\partial\alpha_r = \partial\omega_i/\partial\beta_r = 0$ while $\partial\omega_r/\partial\alpha_r$ and $\partial\omega_r/\partial\beta_r$ have real values: X/t and Y/t, respectively. Furthermore, by differentiating the growth rate $\psi_i^{\star}$ with respect to X/t and Y/t, it is easy to show that (although in general α and β are complex at saddle points) maxima of the growth rate (20) occur for saddle points where $\alpha_i = \beta_i = 0$, and are given by maxima of the ω_i-surface given by real α and β. Because the saddle points that contribute the largest growth rates are also maxima of the temporal dispersion relation, both the maximum growth and direction of maximum growth are simply given by the temporal eigenvalue with the largest value of ω_i for real α and β, say α_m and β_m. For this eigenvalue, the maximum value of $\psi_i^{\star}$ is given by

$$\omega_{im} = \psi_{im}^{\star} \equiv \max\left[\omega_i(\alpha_m, \beta_m)\right]. \tag{21}$$

The direction of maximum growth is given by

$$\frac{X}{Y} = \frac{\partial\omega_r/\partial\alpha_r}{\partial\omega_r/\partial\beta_r} = -\frac{\partial\beta_r}{\partial\alpha_r}, \tag{22}$$

evaluated at the maximum eigenvalue.

2.4. Comparison with existing methods

2.4.1. The Cebeci–Stewartson e^n-method

Cebeci and Stewartson [6] also use the steepest-descent method (from a spatial viewpoint) to evaluate the growth rates within a three-dimensional boundary layer (the von Kármán flow, which is the steady axisymmetric incompressible flow due to an infinite disk rotating in still fluid; von Kármán [19]). Their method is normally applied to boundary layers that are non-parallel (the problems associated with this are discussed in Section 3.4), but with the assumption that these flows are locally parallel. Here, the method is applied to a strictly parallel boundary layer. They chose to restrict their attention to harmonic (fixed real frequency) excitation and to use the steepest-descent method to evaluate one integral, rather than two, of a double, rather than triple, inversion. Therefore, they evaluate fixed-frequency wave packets at large X. Their saddle-point condition gives complex α and β for a fixed ω_r, from which the growth rates along $[Y/X]$-rays are calculated. These growth rates must then be maximized over all ω_r. Thus, their double inversion is of the following form:

$$w(z; x, y, t) = \frac{e^{-i\omega_r^{\circ} t}}{(2\pi)^2} \int_A \int_B \Gamma e^{i[\alpha+\beta Y/X]X}\, d\beta\, d\alpha, \tag{23}$$

where ω_r° is prescribed and Γ is a determinate function of z, α and β for given ω_r° (and R). The α-inversion is performed first, using the residue theorem, leaving the β-integral to be evaluated using the steepest-descent method with Y/X constant as $X \to \infty$. Saddle points in the β-plane are denoted by $\beta^\star$, which give $\alpha^\star = \alpha(\beta^\star)$. The saddle-point condition for given ω_r° is

$$\left.\frac{\partial \alpha_r}{\partial \beta_r}\right|_{\beta^\star} = -\frac{Y}{X}, \qquad \left.\frac{\partial \alpha_i}{\partial \beta_r}\right|_{\beta^\star} = 0, \tag{24}$$

and the spatial growth rate along $[Y/X]$-rays is

$$-\alpha_i^\star - \frac{\beta_i^\star Y}{X}. \tag{25}$$

If the boundary layer is strictly parallel then the saddle-point condition (24) is correct and applies to the entire flow. However, the Cebeci–Stewartson method, applied as it is here to a parallel boundary layer, is overly complicated. As with the essentially temporal method described in Section 2.3, it is not necessary to find the saddle-point contributions for all prescribed ω_r°, and then to maximize over all these contributions, to find the maximum growth rate. If the point impulse response is calculated rather than the response to monochromatic excitation, then all frequencies are excited simultaneously. In a similar way to the temporal formulation in Section 2.3, a second saddle-point condition is then required that is valid at large X and constant t/X. The saddle points are then $\beta^\star$ and $\omega^\star$, where $\alpha(\beta^\star, \omega^\star) = \alpha^\star$, and the two saddle-point conditions are

$$\left.\frac{\partial \alpha}{\partial \beta}\right|_{\beta^\star,\omega^\star} = -\frac{Y}{X}, \qquad \left.\frac{\partial \alpha}{\partial \omega}\right|_{\beta^\star,\omega^\star} = \frac{t}{X}, \tag{26}$$

and the spatial growth rate along rays is

$$\frac{\omega_i^\star t}{X} - \alpha_i^\star - \frac{\beta_i^\star Y}{X}. \tag{27}$$

By differentiating the growth rate with respect to Y/X and t/X, it is shown that the maximum spatial growth rate occurs for the particular saddle point where $\beta_i = \omega_i = 0$ and is given by $-\alpha_i^\star$. The direction of maximum growth is given by Y/X evaluated at this saddle point. The maximum spatial-growth saddle point coincides with the minimum in the $\alpha_i(\beta_r, \omega_r)$-surface of the purely spatial dispersion relation. Thus, the maximum spatial growth rate (in the downstream direction) is

$$-\alpha_{im} \equiv \max\left[-\alpha_i(\beta_r, \omega_r)\right]. \tag{28}$$

So, with both the temporal and the spatial approaches, for a parallel flow it is not necessary to find simultaneous solutions of the dispersion relation and of the saddle-point condition; the result of the steepest-descent analyses is that it is enough to find either the temporal or spatial maximum given by either (21) or (28), respectively.

2.4.2. Spatial versus temporal

In Section 2.3 the steepest-descent method is used from a temporal viewpoint, i.e. the growth rate is maximized at constant t (considering the relative growth rates of the wave packet at all positions in space at a fixed instant in time) and it is found that the maximum temporal growth rate is given by (21) for which $\alpha_i = \beta_i = 0$. The Cebeci–Stewartson method is spatial, i.e. the growth rate is maximized at constant x (considering the relative growth rates of the wave packet at all t and y at a fixed x-position) and it is found that the maximum spatial growth rate is given by (28) for which $\omega_i = \beta_i = 0$. The maximum temporal and spatial

growth factors ($\omega_{im}t$ and $-\alpha_{im}X$, respectively) are not the same; see Gaster [20] and Brevdo [21]. Conversion of the maximum temporal growth rate to a spatial growth rate using the group velocity at the point of maximum temporal growth (which is purely real) under-predicts the maximum spatial growth rate. The discrepancy is given by

$$\omega_{im}/U_m - (-\alpha_{im}) = \omega_{im}/U_m - \max\left[\omega_i^\star/U^\star\right] < 0, \tag{29}$$

where $U_m = (\partial\omega/\partial\alpha)|_{\alpha_m,\beta_m}$ and $U^\star = (\partial\omega/\partial\alpha)|_{\alpha^\star,\beta^\star}$. Examples of this discrepancy are given in Section 2.6, but is usually small in boundary-layer flows; see Gaster [22].

2.4.3. Mack's e^n-method

In the e^n-method proposed by Mack [5] (for a swept wing of infinite span) it is assumed *a priori* that β_i is everywhere zero (where x and y are the chordwise and spanwise directions, respectively), and again disturbances with fixed real frequency are considered. Mack assumes that there is only growth in the x-direction, given by $-\alpha_i$. The Cebeci–Stewartson method shows that $-\alpha_i$ maximized over β_r and ω_r ($\beta_i = \omega_i = 0$) does in fact give the magnitude of the maximum spatial growth even when growth in the y-direction is not excluded *a priori*. However, Mack's method alone does not give the direction of maximum growth correctly, which is given by (24).

2.5. Numerical integration of the impulse response

Here a numerical-integration method, similar that described by Spooner and Criminale [23], is used to calculate the impulse response given by (12). As before, to find the discrete response to localized point forcing, the ω-inversion is performed first using the residue theorem, giving Eq. (13). Further, Θ_j is taken as unity because the exponential terms dominate the growth and because this degree of approximation is consistent with existing e^n-methods. Instead of deforming the A- and B-contours on to steepest-descent paths to collect the dominant time-asymptotic contributions, the α- and β-integrals are approximated by Fourier series, giving the vertical perturbation velocity as

$$w(x, y, t) \simeq \frac{H(t)}{(2\pi)^2 i} \sum_{m=-\infty}^{+\infty} \sum_{n=-\infty}^{+\infty} \sum_{j=1}^{M} e^{i(m\Delta\alpha X + n\Delta\beta Y - \omega_j(\alpha,\beta)t)}, \tag{30}$$

which is evaluated numerically. Here α and β are real, representing the integrations along the A- and B-contours lying on the respective real axes. The physical solution is given by the real part of (30). The initial disturbance excites all possible modes of behaviour but, in practice, the α- and β-summations are limited to ranges that include all the unstable responses, i.e. those giving positive values of ω_i. The numerical-integration method does not involve making a time-asymptotic approximation, but the neglect of most of the damped modes and the continuous spectra causes inaccuracies in the wave-packet representation at short times after the inception of the disturbance, before the damped modes have had a chance to die away. Nonetheless, the results do in principle apply at all other times.

Clearly, it is desirable to restrict the calculations to lie within the spatial regions that are unaffected by aliasing. This unaffected range increases with decreasing stepsize in α and β, but reduction of the stepsize increases the number of calculations required. One source of inaccuracy of this solution scheme is the representation of the integrals by truncated series. The truncation produces ringing, which is characterized by small amplitude waves that appear to propagate outwards from the wave packet especially at short times. These distortions decrease with increasing time as growth of the amplitude coefficients smoothes the ends of the Fourier spectrum.

2.6. Results and comparisons

Although $\partial\omega/\partial\alpha$ and $\partial\omega/\partial\beta$ are in general complex, the real parts alone are often called the group velocities in the x- and y-directions, respectively, and used to determine the direction and magnitude of the propagation velocity. However, as discussed by Briggs [10] and Lingwood [15], this definition of the group (or propagation) velocity of a wave packet can give quite incorrect results when applied to systems that can support unstable waves. The group velocity can be defined unambiguously by saddle points of the complex phase function through which the integration contours of the impulse response can be made to pass, where $\partial\omega/\partial\alpha$ and $\partial\omega/\partial\beta$ are necessarily purely real. Briggs [10] shows that the integration contour can always be deformed through a maximum-growth saddle point corresponding to the dominant asymptotic component of the wave packet. This is because the maximum-growth saddle point lies on the real α- and β-axes, and the associated branch point in the ψ-plane is equivalent to the maximum in the $\omega_i(\alpha_r, \beta_r)$-surface, i.e. ψ_i at the branch point is equal to ω_{im}. No poles can have crossed the real α- and β-axes for $\psi_i > \omega_{im}$, and the coalescing poles that form the saddle point of $\psi(\alpha, \beta)$ on the real α- and β-axes pinch (i.e. separate into the distinct halves of the α- and β-planes as $\psi_i \to \infty$), which is a necessary condition for the steepest-descent path to be deformable through the saddle point. For example, *figure 2* shows the mapping from the complex ψ-plane of the steepest-descent path (S) that passes through the maximum-growth saddle point ($\alpha^\star \approx 0.12$, $\beta^\star \approx 0.29$, $\omega^\star \approx 0.19 + 0.0012i$, $X/t \approx 0.82$ and $Y/t \approx 0.16$), for $R = 60$, to the α- and β-planes. By definition, the steepest-descent path has constant ψ_r and a maximum value of ψ_i at the branch point that maps to the saddle points in the α- and β-planes. Each value of ψ on S (apart from the branch point itself) maps to two values of both α and β (given by $\alpha(\psi_S)$ and $\beta(\psi_S)$, respectively): one each side of the saddle point. The line marked by R in the ψ-plane, when mapped to the α- and β-planes, gives the heights of the saddle points and therefore bounds valleys of ψ_i through which the steepest-descent paths must pass. The high-ground relative to the saddle points is given by Q and the mappings $\alpha(\psi_Q)$ and $\beta(\psi_Q)$. *Figure 2* confirms that the A- and B-contours which lie on the real α- and β-axes can be deformed onto the steepest-descent paths and therefore $\partial\omega/\partial\alpha$ and $\partial\omega/\partial\beta$ at the saddle points accurately give the components of the group velocity.

Normally when performing a saddle-point analysis it would be necessary to find simultaneously solutions of the dispersion relation and the saddle-point condition. However, because the maximum temporal-growth saddle point of the phase function coincides with the eigenvalue of the temporal dispersion relation with the maximum in the $\omega_i(\alpha_r, \beta_r)$-surface, it is not necessary to incorporate a saddle-point condition in the eigenvalue code if only the maximum is required; it is enough to find temporal eigenvalues. For example, *figures 3–5* show contours of ω for $R = 60$, $R = 150$ and $R = 500$. The maxima in ω_i, i.e. ω_{im} defined by (21), are marked. In all cases, the lines of zero $\partial\omega_i/\partial\alpha_r$ and $\partial\omega_i/\partial\beta_r$ both pass through ω_{im}, which indicates that as expected $\partial\omega/\partial\alpha$ and $\partial\omega/\partial\beta$ are purely real at the maxima, and the saddle-point condition is satisfied there. The directions of maximum growth are given by (22) evaluated at these maxima. For $R = 150$, in *figure 4*, the Ekman layer has two unstable modes: one is viscously unstable and is often referred to as a type-2 instability, the other is inviscidly unstable and is referred to as a type-1 instability. Type-2 instability dominates at low Reynolds numbers while type-1, the most unstable wave of which has negative wave angle ($\tan^{-1}(\beta_r/\alpha_r)$), dominates as $R \to \infty$. At $R = 150$, type-1 is more unstable than type-2. Although the phase speeds and orientation of the wave fronts are different, it will be shown that where the two instability modes coexist both contribute to a single wave packet because the group velocities are similar. It has already been stated that the integration contour can always be deformed through a maximum-growth saddle point, which for $R = 150$ corresponds to the type-1 maximum in *figure 4*, but it is not obvious that the integration contour can also be made to pass through the second maximum to give the type-2 contributions to the impulse response. However, *figure 6* shows that the integration contour can be deformed through both saddle points and be joined to the real α- and β-axes within valleys. The shaded regions indicate the high-ground relative to the two saddle points (denoted by $\circ$ and $\times$) and

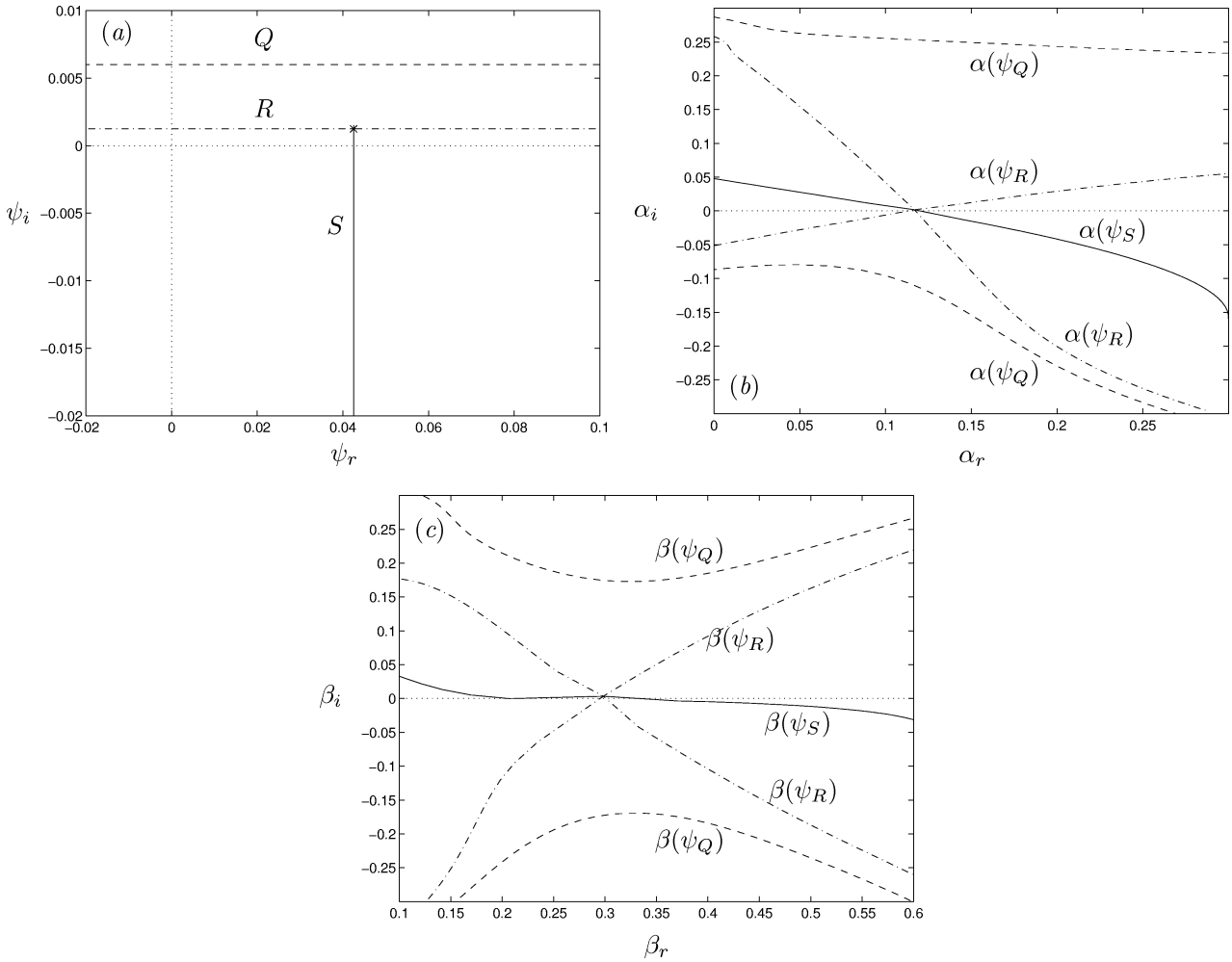

Figure 2. Mapping of the steepest-descent path (S) from (a) the ψ-plane to (b) the α-plane, with $\beta = \beta^\star$, and (c) the β-plane, with $\alpha = \alpha^\star$. The height of the saddle point (R) and the high-ground relative to the saddle point (Q) are marked by $\alpha(\psi_R)$ and $\beta(\psi_R)$, and $\alpha(\psi_Q)$ and $\beta(\psi_Q)$, respectively. The Reynolds number is 60 and the chosen saddle point gives the largest growth at this Reynolds number.

mappings of the steepest-descent paths (S_1 and S_2 for the type-1 and type-2 saddle points, respectively) from the ψ-plane to the α- and β-planes are given by the solid and dashed lines. In the α-plane, $\beta = \beta_1^\star$ ($\beta = \beta_2^\star$) for all the solid (dashed) lines; similarly, in the β-plane, $\alpha = \alpha_1^\star$ ($\alpha = \alpha_2^\star$) for all the solid (dashed) lines. The dashed-dotted lines are a schematic representation of the two steepest-descent paths being joined together, and of the paths being joined to the real axes, within the valleys of both saddle points. Thus, the two maxima of the temporal sheet of the dispersion relation in *figure 4* for $R = 150$ give the maximum growth and direction of maximum growth of the type-1 and type-2 instability components of the single wave packet.

Ideally, a comparison between the steepest-descent results and a numerical solution of the full linearized stability equations should be made to show the extent to which the steepest-descent method captures the growth of the wave packet. However, numerical calculations of this sort are beyond the scope of the current work and are left for the future. Nevertheless, for $R = 60$, $R = 150$ and $R = 500$ and a selection of times, the wave packets resulting from a impulsive point source have been calculated using the numerical-integration method described in Section 2.5. Unlike the steepest-descent method, the numerical-integration solution is not an asymptotic

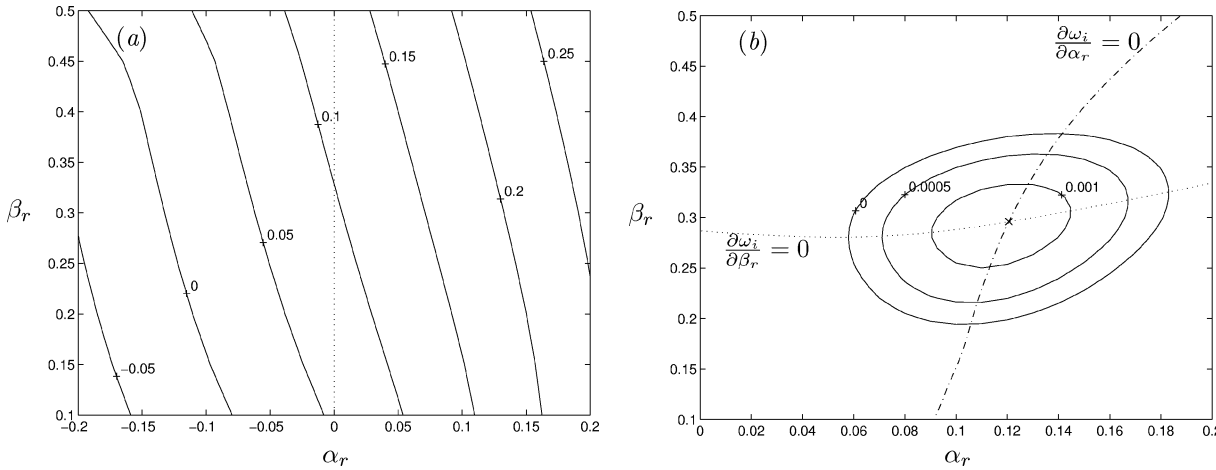

Figure 3. Contours of (a) ω_r and (b) ω_i, for $R = 60$ and $\alpha_i = \beta_i = 0$.

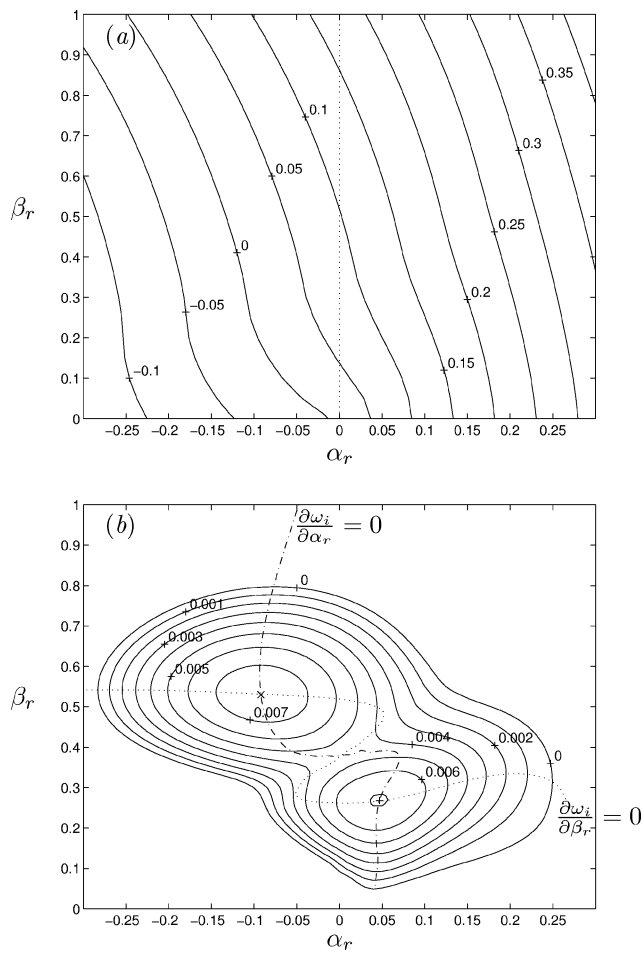

Figure 4. Contours of (a) ω_r and (b) ω_i, for $R = 150$ and $\alpha_i = \beta_i = 0$. The maxima marked by $\times$ (type-1) and $+$ (type-2) have values of approximately 0.00765 and 0.00705, respectively.

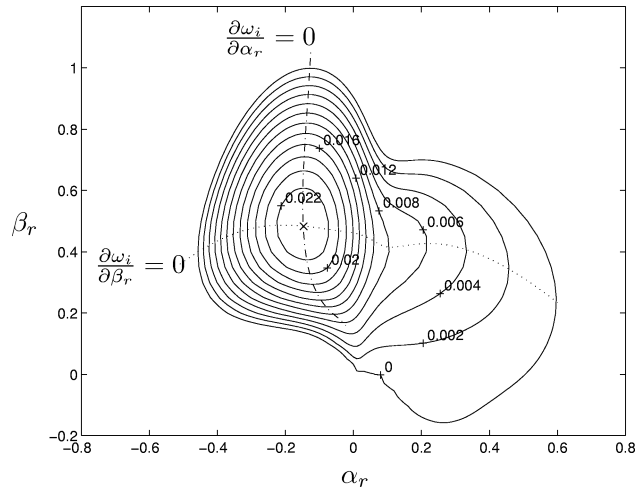

Figure 5. Contours of ω_i for $R = 500$ and $\alpha_i = \beta_i = 0$.

solution (although it is not accurate at very small times after the impulsive disturbance). *Figure 7* shows views of the wave packets at the three chosen Reynolds numbers. The orientation of the wave fronts of the type-1 and type-2 components of the wave packets are clearly visible. Type-2 has positive wave angle and is damped by $R = 500$; type-1 has negative wave angle and is dominant by $R = 150$. Note that with increasing time, the shape of the wave packets approaches an ellipse, with the wavefronts aligned with the major axis.

Here, the maximum growth and direction of maximum growth predicted by the steepest-descent arguments are compared with the growth and propagation of the entire wave packet calculated using numerical integration. The numerically-integrated wave packet could be used to determine the maximum temporal growth (to be compared with (21)) or the maximum spatial growth (to be compared with (28)), depending on whether the amplitude of the wave packet is maximized over all x and y for a given t or whether the amplitude is maximized over all y and t for a given x. The former approach is taken here. *Figure 8* shows contours of the peak-normalized envelope function of the numerically-integrated wave packets compared with the directions and spatial positions at the chosen times of the maxima of the wave packets predicted by (22). In each case, the contour levels of the peak-normalized envelope function range from 0.1 to 0.9. For $R = 150$, in *figure 8(b)*, the contour levels are not monotonic, therefore shading has been added to indicate the amplitude. White represents zero amplitude; black indicates unit amplitude. *Figure 9(a)* shows a more detailed comparison for $R = 60$. The exact positions of the maxima of the numerically-integrated wave packets at eight chosen times ($\circ$) are given. The solid line is not a line of best fit, but is (as in *figure 8(a)* the direction of propagation predicted by (22), and the positions of the maxima at the same times are marked by $\times$. Although (22) is based on a time-asymptotic approximation of the impulse response, the agreement shown here (and in *figure 8*) with the results from the numerical-integration method are good for t as low as 250. In *figure 9(b)*, rather than comparing direction of propagation and position of maxima, the maximum amplitudes predicted by (21) are compared with those given by the numerical-integration method. (The non-dimensional time has been scaled by R because the dimensional time is proportional to tR for fixed viscosity and freestream velocity.) For the method based on steepest descent, $\ln(A_m/A_0)$, where A_0 is the amplitude at $t = 0$ and A_m is the (time dependent) maximum amplitude, is given simply by $\omega_{im}t$. For the numerically-integrated wave packet, $\ln(A_m/A_0) = \ln(\max[e(x, y; t)]) - \ln A_0$, where $e(x, y; t)$ is the envelope function calculated from $w(x, y, t)$ given by (30) and A_0 is the initial amplitude. Because A_0 is arbitrary, the numerically-integrated curves of $\ln(A_m/A_0)$ can be shifted vertically and gradients should be compared in *figure 9(b)*. Normally in calculations of the n-factor for non-parallel flows amplitudes

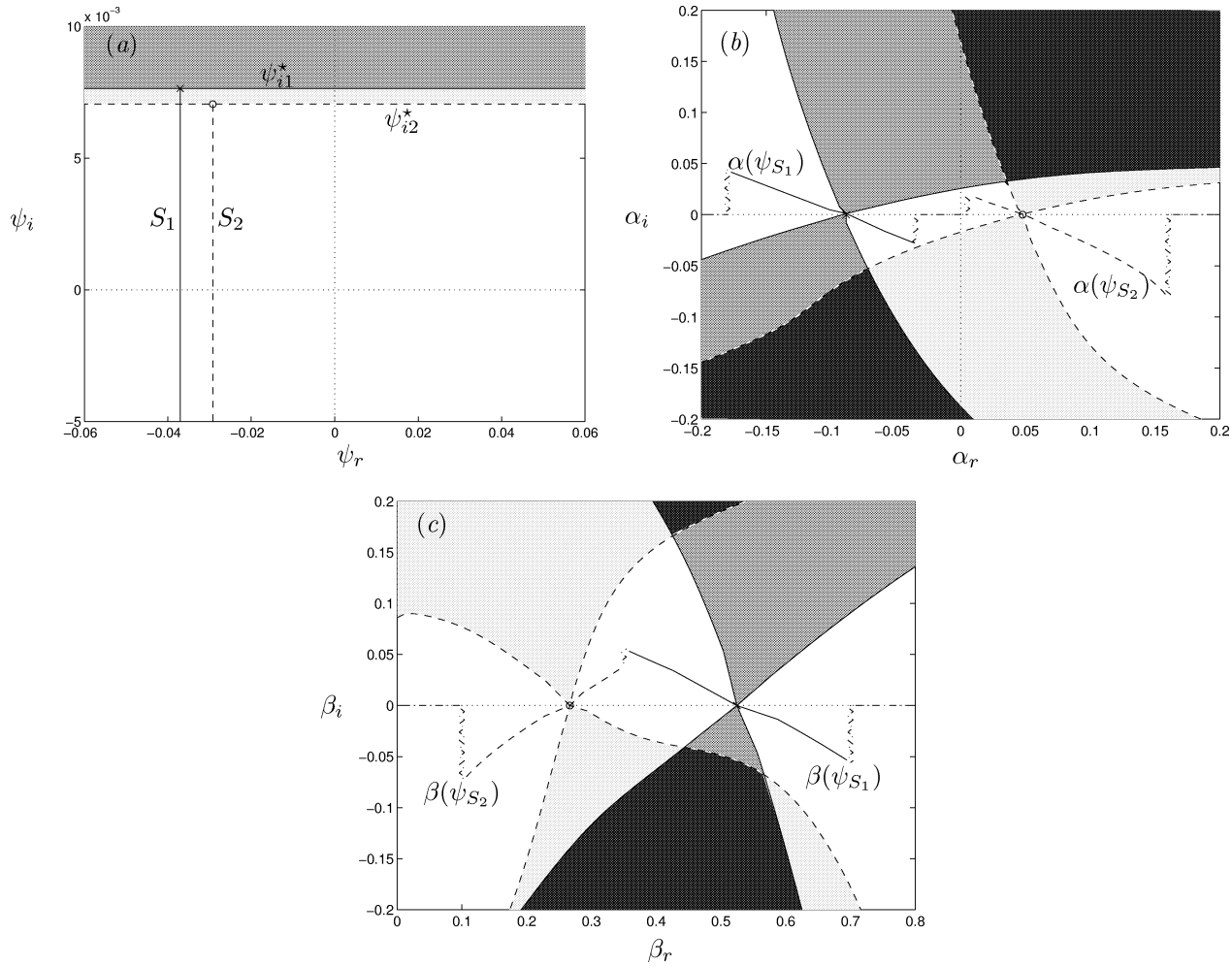

Figure 6. Mapping of the steepest-descent paths (S_1 and S_2) from (a) the ψ-plane to (b) the α-plane, with $\beta = \beta_{1,2}^\star$, and (c) the β-plane, with $\alpha = \alpha_{1,2}^\star$, for $R = 150$ showing the two largest-growth saddle points corresponding to the two instability modes. In (b) and (c) the high-ground relative to the saddle points, where $\psi_i > \psi_{i1,2}^\star$, is denoted by the areas with pale and medium shading, respectively; the darkest shading indicates overlapping high-ground. The dashed-dotted lines indicate schematically joining the two steepest-descent paths to each other in the central valleys in the α- and β-planes, and to the respective real axes as $\alpha_r \to \pm\infty$ and $\beta_r \to \pm\infty$.

are normalized by the amplitude at the first neutral point. However, for the parallel Ekman layer the whole flow is either stable, neutral or unstable (i.e. growth rates do not vary with time or position). The three Reynolds numbers considered here are all unstable to varying degrees, disturbances grow uniformly fast from their inception and, therefore, the numerical values of $\ln(A_m/A_0)$ are, in general, larger than normal (non-parallel) n-factors for which there are regions of decay and relatively slow growth. The numerically-integrated amplitude ratios can decrease in magnitude close to the initiation point due to dispersion of the wave packet, but as expected they asymptote to $\omega_{im}t$ as $t \to \infty$.

A comparison between the maximum spatial and temporal growth rates shows close agreement. For example, for $R = 60$, $\omega_{im} \approx 0.001245$, where $U_m \approx 0.8250$. At this Reynolds number, the maximum spatial growth rate is $-\alpha_{im} \approx 0.001531$. Thus, conversion of the maximum temporal growth rate to a spatial one, as described by (29), would result in a small discrepancy of about 1.5%. At $R = 150$ the discrepancy is less than 0.8%.

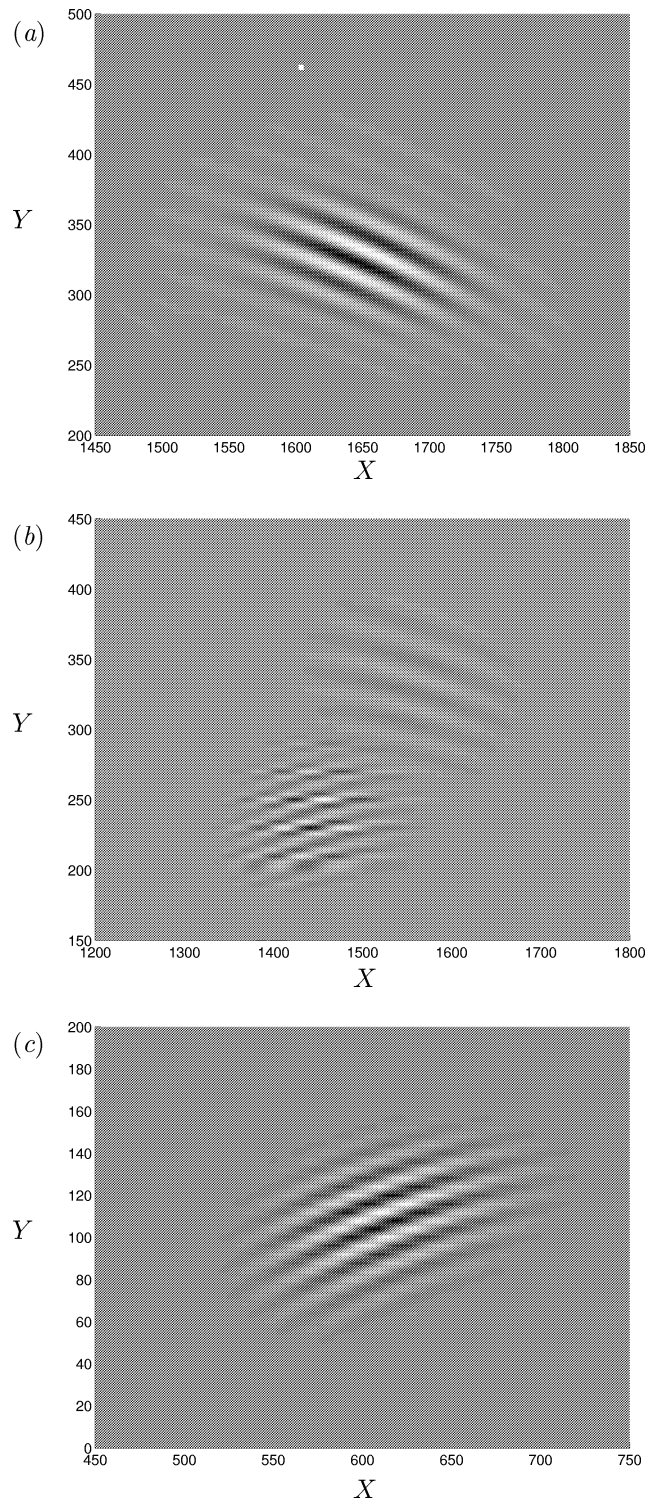

Figure 7. Views of the peak-normalized wave packets, evaluated using numerical integration, showing the orientation of the wave fronts within the packets: (a) $R = 60$ and $t = 2000$, (b) $R = 150$ and $t = 2000$, (c) $R = 500$ and $t = 1000$.

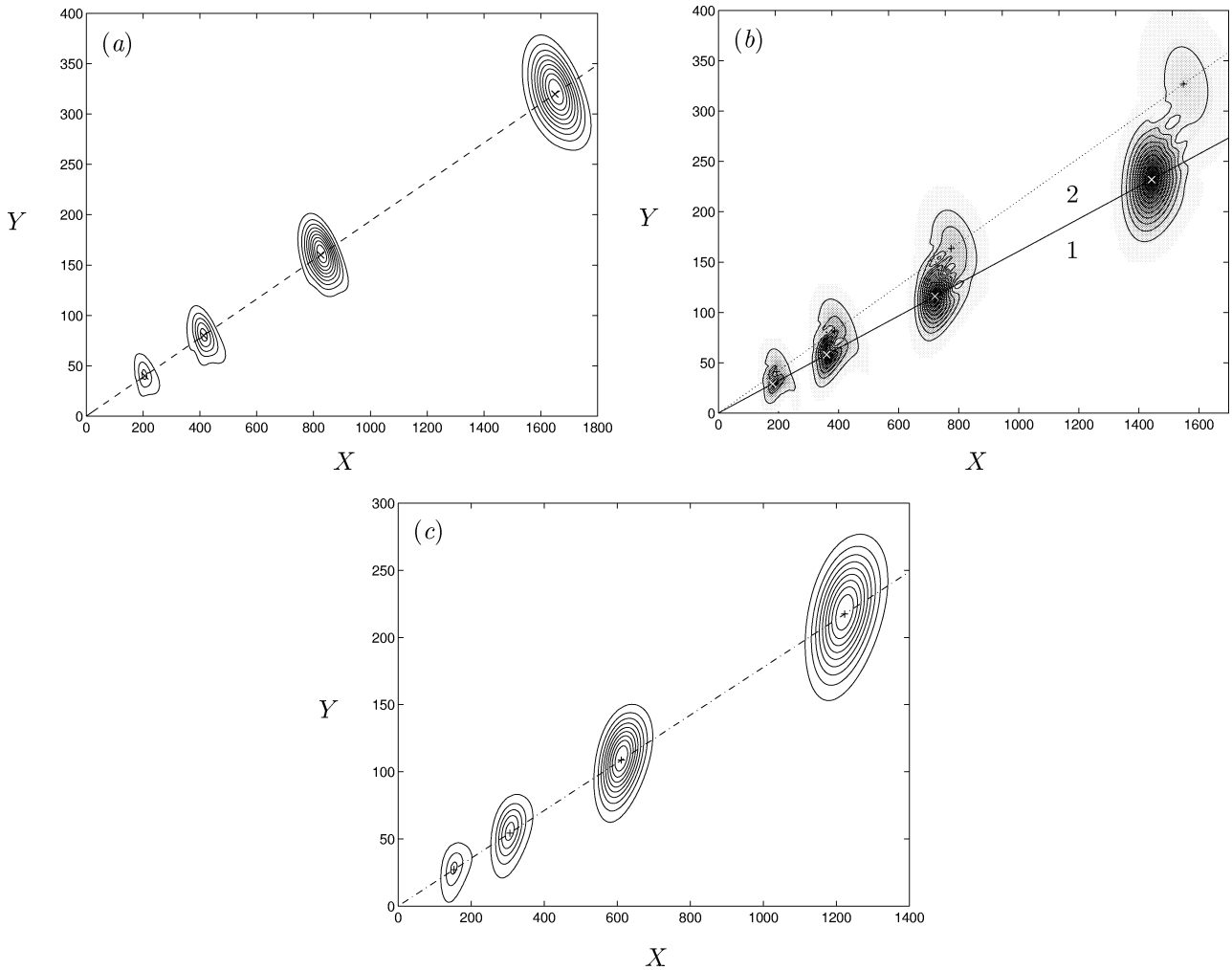

Figure 8. Contour plots of the peak-normalized envelope function of the wave packet, evaluated using numerical integration, at $t = 250, 500, 1000, 2000$: (a) $R = 60$, (b) $R = 150$, (c) $R = 500$. The constant gradient lines give the direction of propagation in the (x, y)-plane, with increasing time, predicted by (22) and the symbols give the predicted positions of the maxima of the wave packets at $t = 250, 500, 1000, 2000$. For $R = 150$, the propagation of both type-1 (labelled 1) and type-2 (labelled 2) components of the wave packet are predicted.

As discussed in Section 1, it is worth noting that, although the maxima in the wave packets are always convective, above a critical Reynolds number there is an absolute instability in the y-direction, which is characterized by growth with increasing time at fixed y-positions. This is shown in *figure 10(b)* for $R = 500$ compared with the purely convective behaviour of the whole wave packet for $R = 60$, in *figure 10(a)*. The difference between *figure 8(c)* and *figure 10(b)* is that in the latter the envelope function is not peak normalized, and therefore the relative magnitudes of the wave packets at subsequent time instants can be compared. The absolute instability is predicted by Lingwood [13] to occur for $R > 198$ for the Ekman layer.

2.7. Summary

Comparison with a numerical-integrated impulse response has shown that the maximum temporal growth and the direction in which that maximum growth occurs in the parallel Ekman boundary layer are both

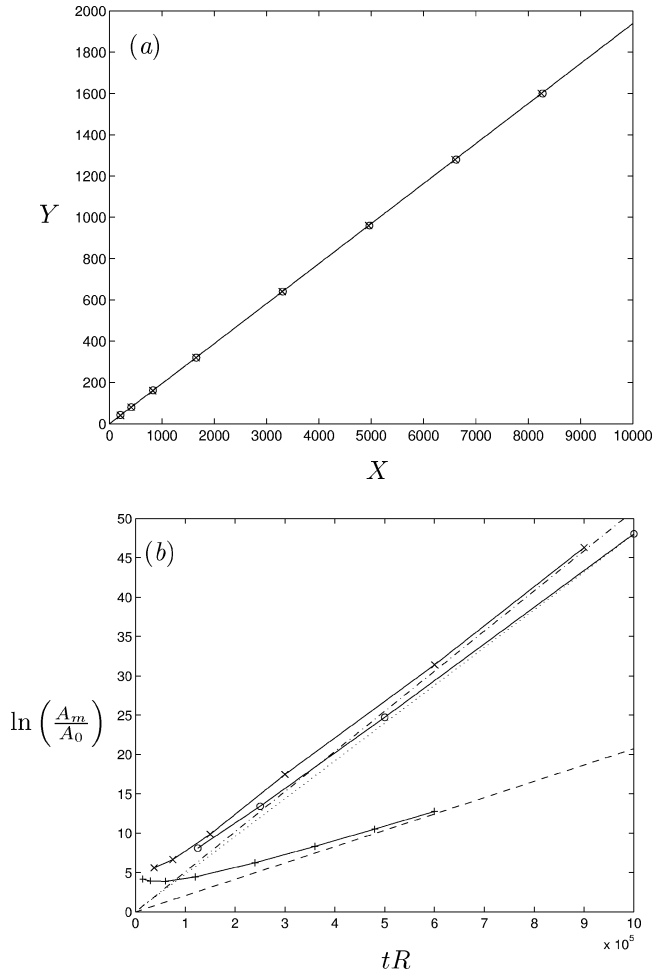

Figure 9. (a) Direction of propagation in the (x, y)-plane of the maximum of the wave packet, for $R = 60$, predicted by (22) (——), positions of the maxima at eight values of t ($\times$), and positions of the maxima at the same t calculated by numerical integration ($\circ$). (b) Maximum amplitude ratio A_m/A_0 predicted by (21) ((– – –) $R = 60$; (— · — ·) $R = 150$; ($\cdots$) $R = 500$) compared with values calculated using numerical integration ((+) $R = 60$; ($\times$) $R = 150$; ($\circ$) $R = 500$), which can be shifted vertically depending on the initial amplitude of the disturbance.

accurately predicted by the time-asymptotic impulse response. However, it must be borne in mind that for some flows transition may occur within the transient regime before the asymptotic solution becomes valid, which would imply that the asymptotic method for calculating n-factors is of no practical use. To clarify this point comparison with experiments with the particular flow of interest is required. Assuming that the asymptotic method becomes valid before transition, the maximum temporal growth rate predicted by the time-asymptotic impulse response is simply given by the maximum in the temporal surface of the dispersion relation $\omega_i(\alpha_r, \beta_r)$. The growth of coexisting inviscid and viscous instability mechanisms can be easily monitored due the separation of the respective ω_i-maxima in the (α_r, β_r)-plane.

The spatial e^n-method proposed by Cebeci and Stewartson [6] has been considered. Maximization of the spatial growth over all monochromatic excitation is equivalent to calculating the maximum spatial growth of the impulse response. If just the maximum is required, there is no need to calculate the whole impulse response, i.e. no need to allow α, β and ω to take complex values and to solve the governing equations for simultaneous spatial saddle points and eigenvalues of the dispersion relation. The maximum spatial growth occurs for the

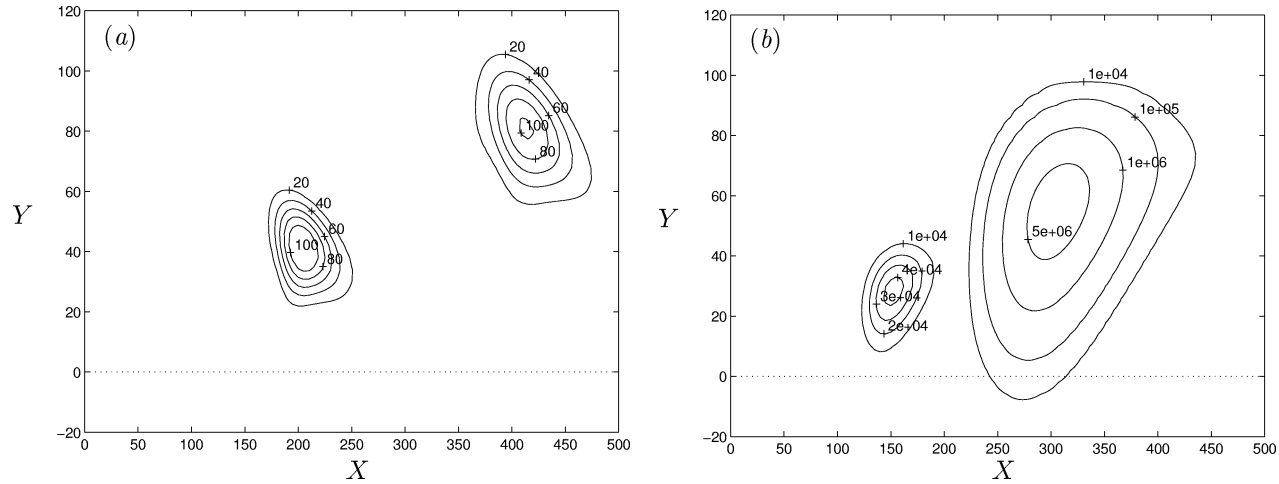

Figure 10. Contour plots of the envelope function (not peak-normalized) of the wave packet, evaluated using numerical integration, at $t = 250$ and $t = 500$: (a) $R = 60$, (b) $R = 500$. At $R = 500$ the flow is absolutely unstable in the y-direction.

particular spatial saddle point for which $\beta_i = \omega_i = 0$, which coincides with the maximum in the spatial surface of the dispersion relation $-\alpha_i(\beta_r, \omega_r)$. The difference between the maximum temporal and spatial growths is shown to be small in the given example.

The method proposed by Mack [5], which is spatial but with $\beta_i = 0$, gives the correct value for the maximum growth rate. However, Mack's method does not give the direction of maximum growth because by fixing $\beta_i = 0$ it is assumed that there is growth only in the streamwise direction, which is not the physical reality.

Brevdo [24] proposed a three-dimensional e^n-method for non-parallel boundary layers where, as the Reynolds number varies, the successive maximum growth rates, ω_{im} or $-\alpha_{im}$, are integrated along a piecewise linear curve defined by the R-dependent direction of those successive maximum growth rates, as the Reynolds number varies. This method would be relatively easy because of the simple condition for the direction of maximum growth and the value of that maximum growth, which means that the entire spectrum of unstable waves does not have to be considered. However, the component reaching maximum amplitude in a non-parallel boundary layer at a particular observation position does not have the maximum growth rate at all position upstream of that position. In other words, the amplitude obtained by piecing together successive maximum growth rates does not correspond to the amplitude of a physical disturbance within the boundary layer. Nevertheless, this problem is common to most of the existing three-dimensional e^n-methods to some degree (see Section 3.4) and, therefore, Brevdo's suggestion is perhaps of some use. Indeed, Taylor and Peake [25,26] have discussed and implemented this suggestion, and found distinct advantages over the envelope method and therefore propose that it may be a more useful design tool, particularly when two instability modes are present. Notwithstanding, the rest of this paper is devoted to describing a method that calculates physical maximum amplitudes in growing boundary layers.

3. Non-parallel boundary layers

3.1. Two-dimensional flows—the Blasius boundary layer

Here the two-dimensional non-parallel Blasius boundary layer is used to illustrate how a method based on the impulse response of a growing boundary layer can be used to calculate the maximum disturbance amplitude at

a given downstream position and, therefore, to calculate the n-factor. Here, only two-dimensional disturbances are considered, i.e. $\beta = 0$.

The quasi-parallel approach is applied to the boundary layer, giving modal solutions of the form

$$u(x, z, t) = A_0 \hat{u}(x_1, z) e^{-i\Psi(x,z,t)X}, \tag{31}$$

where z is the wall-normal direction, $X = x - x_0$ and

$$\Psi(x, z, t) = -\frac{1}{X}\left[\int_{x_0}^{x} \alpha(x_1)\, dx - \omega(x_1)t\right]; \tag{32}$$

similarly for $v(x, z, t)$. Here $x_1 = \varepsilon x$, where ε is a small quantity identified with R^{-1}. The growth of the boundary layer is governed by the slow scale x_1, and the ω has been written as a function of x_1 to emphasize the fact that $\partial(\Psi X)/\partial x = \alpha$ just as for a parallel flow. In the quasi-parallel approximation the slow-scale-dependent amplitude cannot be determined and therefore is set to the initial amplitude A_0 and contributions to the amplitude are due only to the imaginary part of the phase function Ψ. (This simplification is what distinguishes the quasi-parallel approximation from the zeroth-order solution of the truly non-parallel approach based on multiple-scales theory; see Mack [27].) The mean flow is given by the locally parallel Blasius similarity solution and the eigenvalues α and ω satisfy a local dispersion relation, i.e. a different eigenvalue problem (of the Orr–Sommerfeld equation) must be solved at successive x-positions because of the change in boundary-layer thickness. The eigenvalues at successive x-positions must be related such that they represent the propagation of a physical wave through the boundary layer. In steady boundary layers, the dimensional frequency is in fact constant as a wave propagates.

Consider the response to an impulsive forcing of the form

$$w(0; x, t) = \delta(X)\delta(t), \tag{33}$$

which is given by

$$w(z; x, t) = \frac{1}{(2\pi)^2} \int_W \int_A \frac{\Phi}{\Delta_0} e^{-i\Psi X}\, d\alpha\, d\omega, \tag{34}$$

where, as with (12), Φ is a function of z and A and W are the inversion contours in the α- and ω-planes, respectively. Note that for the Blasius boundary layer the non-dimensionalizing velocity, length, pressure and time scales are $U^*_\infty \equiv U^*(z \to \infty)$ (which is independent of x), δ^*, $\rho^* U^{*2}_\infty$ and δ^*/U^*_∞, respectively, where δ^* is the displacement thickness and, as before, asterisks denote dimensional quantities. Clearly, the displacement thickness is a function of position, which to four decimal places takes the following form:

$$\delta^* = 1.7208 l^*, \tag{35}$$

where $l^* = (\nu^* x^*/U^*_\infty)^{1/2}$, ρ^* and ν^* being the fluid density and viscosity, respectively. The Reynolds number is based on the displacement thickness, i.e. $R = U^*_\infty \delta^*/\nu^*$. The form of the non-dimensionalizing time scale implies that a constant dimensional frequency ω^* has varying dimensionless ω in the x-direction. For this reason it is usual to introduce a scaled frequency

$$f = \frac{\omega}{R} = \frac{\omega^* \nu^*}{U^{*2}_\infty}, \tag{36}$$

which is constant in x for constant dimensional frequency.

The α-inversion of (34) is performed first using the residue theorem leaving α as a function of ω, as well as x. In general there will be residue contributions from poles in both the upper and lower halves of the complex α-plane, which correspond to physical responses in the $X > 0$ and $X < 0$ regions, respectively. For the Blasius boundary layer it is well known that there is only one *unstable* mode (the Tollmien–Schlichting (TS) mode), which is convectively unstable in the downstream direction, and there is no absolute instability. Therefore, here only the impulse response due to the TS mode for $X > 0$ is considered. As $X \to \infty$ with t/X constant, the asymptotic impulse response is dominated by contributions from the saddle points of Ψ, i.e. contributions from frequencies that satisfy $\partial\Psi/\partial f = 0$, which implies that, in dimensional terms,

$$\int_{x_0^*}^{x^{\star *}} \frac{\partial \alpha^*(x^*, \omega^{\star *})}{\partial \omega^*}\, dx^* = t^*, \tag{37}$$

or in dimensionless terms,

$$\frac{2}{1.7208^2} \int_{R_0}^{R^\star} \frac{\partial \alpha(R, f^\star)}{\partial f}\, dR = T, \tag{38}$$

where $T = tR = t^* U_\infty^{*2}/\nu^*$ and frequencies that satisfy (37) or (38) are denoted by a $\star$-superscript and $\omega^{\star *}$ ($f^\star$) is kept constant during the integration over x^* (R). The saddle-point condition (38) gives the time that a given frequency wave takes to travel between the two fixed points R_0 and $R^\star$. This time must be real and, therefore, the imaginary part of the integral (38) must be zero, namely

$$\frac{2}{1.7208^2} \int_{R_0}^{R^\star} \frac{\partial \alpha_i(R, f^\star)}{\partial f_r}\, dR = T_i = 0. \tag{39}$$

However, although this integral between the two given positions is zero, the integrand $\partial\alpha_i/\partial f_r$ at intermediate positions is, in general, non-zero. So, for $R_0 < R < R^\star$, t is complex and is only real at $R = R_0$ (where $T = 0$) and at $R = R^\star$. *Figure 11* illustrates this point for a purely real value of $f^\star \approx 5.22 \times 10^{-5}$ that satisfies (39), $R_0 = 500$ and $R^\star = 2000$. For given R_0 and $R^\star$ there will be many (generally complex) values of $f^\star$ that satisfy (39); each gives a component of the wave packet that arrives at $R^\star$ at a different time. The growth of a component of the wave packet is given by the imaginary part of the phase function ($\Psi^\star \equiv \Psi(f^\star)$), which is given by (32), such that

$$\begin{aligned} \Psi_i^\star X &= \ln\left(\frac{A^\star}{A_0}\right) = f_i^\star T - \frac{2}{1.7208^2}\left[\int_{R_0}^{R^\star} \alpha_i(R, f^\star)\, dR\right] \\ &= \frac{2}{1.7208^2}\left[f_i^\star \int_{R_0}^{R^\star} \frac{\partial \alpha_r(R, f^\star)}{\partial f_r}\, dR - \int_{R_0}^{R^\star} \alpha_i(R, f^\star)\, dR\right], \end{aligned} \tag{40}$$

where A_0 and $A^\star$ are the amplitudes at R_0 and $R^\star$, respectively, and where the real time of travel, given by (38) and (39), has been substituted into the right-hand side.

The growth in (40) can be maximized by differentiating $\Psi_i^\star X$ with respect to T to find which component arriving at $R^\star$ has the largest amplitude compared with the amplitude at R_0, as follows:

$$\begin{aligned} \frac{\partial(\Psi_i^\star X)}{\partial T} &= f_i^\star + T\frac{\partial f_i^\star}{\partial T} - \frac{2}{1.7208^2}\left[\frac{\partial f_i^\star}{\partial T}\int_{R_0}^{R^\star} \frac{\partial \alpha_i(R, f^\star)}{\partial f_i}\, dR\right] \\ &= f_i^\star + \frac{2}{1.7208^2}\left[\frac{\partial f_i^\star}{\partial T}\int_{R_0}^{R^\star} \frac{\partial \alpha_r(R, f^\star)}{\partial f_r}\, dR - \frac{\partial f_i^\star}{\partial T}\int_{R_0}^{R^\star} \frac{\partial \alpha_i(R, f^\star)}{\partial f_i}\, dR\right] = 0. \end{aligned} \tag{41}$$

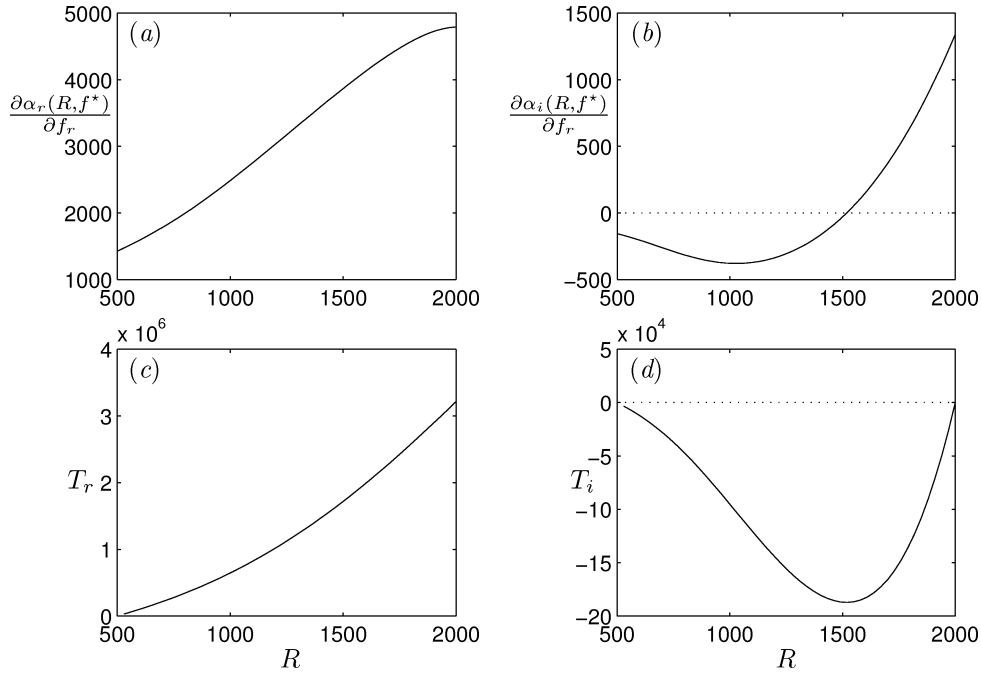

Figure 11. (a) Plot of the real part of the integrand of (38), (b) plot of the imaginary part of the integrand of (38), (c) plot of T_r, (d) plot of T_i, for $R_0 \leqslant R \leqslant R^\star$, where $R_0 = 500$ and $R^\star = 2000$.

The Cauchy–Riemann relations imply the second and third terms of (41) cancel and that, therefore, $f_i^\star = 0$ for the maximum growth given by

$$\Psi^\star_{i\max} X = \max_f \left[\ln\left(\frac{A^\star}{A_0}\right)\right] = -\frac{2}{1.7208^2}\int_{R_0}^{R^\star} \alpha_i\,(R,\, f^\star)\, dR = \bar{n}. \tag{42}$$

Thus, if only the maximum amplitude at a given $R^\star$ is of interest, and not the whole wave packet, then only the purely real value of $f^\star$ that satisfies (39) is required. The maximum amplitude $\Psi^\star_{i\max} X$ is equivalent to a maximization over all frequency (since an impulse excites all frequencies simultaneously) of $\ln(A^\star/A_0)$, i.e. it is an n-factor of sorts and is denoted here by $\bar{n}$, but it is not the usual n-factor because A_0 is defined at x_0 that, as yet, is an arbitrarily chosen position not a neutral point on the lower branch of the neutral curve.

There may be some concern that saddle points have simply been located, without any check on the global topography of the phase function, and that, therefore, there is no firm evidence that the steepest-descent path can actually be deformed through the saddle points. However, as with the parallel boundary layer (Section 2.6), it is possible to show that the steepest-descent path can always be deformed through the particular saddle point that leads to the maximum growth between two points. The maximum-growth saddle point lies on the real frequency axis and the associated branch point in the complex Ψ-plane lies at $\Psi^\star_{\max}$, with imaginary part given by (42). Now, there would be concern about the eligibility of a saddle point if the high-ground relative to it, i.e. the mapping into the complex f-plane of the region where $\Psi_i > \Psi^\star_{i\max}$, crossed the real frequency axis. Imagine a plot of $\Psi_i = -(2/(1.7208^2 X))\int_{R_0}^{R^\star} \alpha_i(R,\, f_r)\, dR$ against f_r ($f_i = 0$), then the maximum of this plot is given by

$$\int_{R_0}^{R^\star} \frac{\partial \alpha_i}{\partial f_r}\, dR = 0, \tag{43}$$

which means that this point on the plot satisfies $t_i = 0$ given by (39) and is in fact $\Psi^\star_{i\max}$. In other words, no other real frequency gives a value of $\Psi_i > \Psi^\star_{i\max}$ and, therefore, the two regions of high-ground in the f-plane originating at the saddle point and extending into opposite half-planes must remain in those half-planes, allowing the steepest-descent path to pass through the saddle point and join the real axis within valleys at the integration limits of the frequency inversion.

Here, results are presented from a code in which, for a given $f_i^\star$ (equal to zero for the maximum amplitude), a Newton–Raphson iteration scheme is used to converge on to a value of $f_r^\star$ that satisfies (39), to within some preset tolerance, starting from an estimated f_r. In *figures 12(a)* and *12(b)* the dashed lines show $\bar{n}$ calculated at the discrete $R^\star$ positions denoted by $\circ$ for $R_0 = 500$ and $R_0 = 2000$, respectively. These plots represent the maximum amplitude within a wave packet generated by an impulsive source at R_0. Here, $f_i^\star = 0$ because only the maximum of the wave packet is of interest. The solid lines show the R-dependent amplitude of the fixed frequency components that reach maximum amplitude at $R^\star$. For $R_0 = 500$, which is in the stable region for the Blasius boundary layer (the critical Reynolds number for convective instability is about 520), all frequency waves must go through a region of decay before reaching the lower branch of the neutral curve where they begin to amplify. Whereas $R_0 = 2000$ lies in the unstable region for certain frequencies and it is particular values of these frequencies that reach maximum amplitude downstream, without going through a region of decay. Thus, $\bar{n}$ is much larger for a given $R^\star$ when $R_0 = 2000$ than when $R_0 = 500$. *Figure 13* shows $\bar{n}$ (as in *figure 12*), $f^\star$ (real) and T plotted against $R^\star$ for $R_0 = 500$ and $R_0 = 2000$. The frequency and time decrease and increase, respectively, with $R^\star$. Clearly, $\bar{n}$ is highly dependent on R_0 and, if these amplitudes are to be used for transition prediction, it is essential to find the value of R_0 that results in the largest amplitude at a given $R^\star$, i.e. to find the worst case. This is discussed below.

Usual e^n-methods compare the amplitude of a disturbance at a given downstream position with its amplitude at the first neutral point. Indeed, it can be shown as follows that $\Psi^\star_{i\max}X$ from (42) has a maximum over all R_0, when R_0 is a neutral point. Let $\Psi^\star_{i\max}X = \psi^\star(R_0, f^\star; R^\star)$, where $f_i^\star = 0$ for maximum growth with respect to T at given $R^\star$ (see (42)), then when

$$\frac{d(\Psi^\star_{i\max}X)}{dR_0} = \frac{\partial\psi^\star}{\partial f_r}\frac{df_r}{dR_0} + \frac{\partial\psi^\star}{\partial R_0} = 0, \tag{44}$$

$\partial\psi^\star/\partial R_0 = 0$ because $\partial\psi^\star/\partial f_r$, in the first term on the right-hand side of (44), is equal to $-T_i$, which is zero for $f^\star$. But differentiating (42) shows that $\partial\psi^\star/\partial R_0 = -(2/1.7208^2)\alpha_i(R_0, f^\star)$ and, therefore, for a given $R^\star$, α is purely real at the value of R_0 leading to the worst case. Hence, for a given $R^\star$, the maximum amplitude with respect to all T and R_0 is given by real $\alpha(R_0, f^\star)$ and $f^\star$; R_0 is a neutral point.

Letting the neutral position (a function of frequency) now be $R_n(f)$ and R_0 be a position farther upstream in the stable region, then the time taken for a disturbance to travel from R_n to the chosen $R^\star$ can be written as

$$\begin{aligned} T &= \frac{2}{1.7208^2}\left[\int_{R_0}^{R^\star}\frac{\partial\alpha(R, f^\star)}{\partial f}\,dR - \int_{R_0}^{R_n(f^\star)}\frac{\partial\alpha(R, f^\star)}{\partial f}\,dR\right] \\ &= \frac{2}{1.7208^2}\int_{R_0}^{R^\star}\frac{\partial\alpha(R, f^\star)}{\partial f}\,dR - \overline{T}(f^\star), \end{aligned} \tag{45}$$

where the two terms that form T are the time to reach $R^\star$ from R_0 and the time to reach R_n from R_0, and are individually complex, but where (for $f^\star$) T itself is real. The limits of integration of the first of these terms are independent of frequency. Hence, if T is to be real, the new saddle-point condition is

$$T_i = \frac{2}{1.7208^2}\int_{R_0}^{R^\star}\frac{\partial\alpha_i(R, f^\star)}{\partial f_r}\,dR - \overline{T_i}(f^\star) = 0, \tag{46}$$

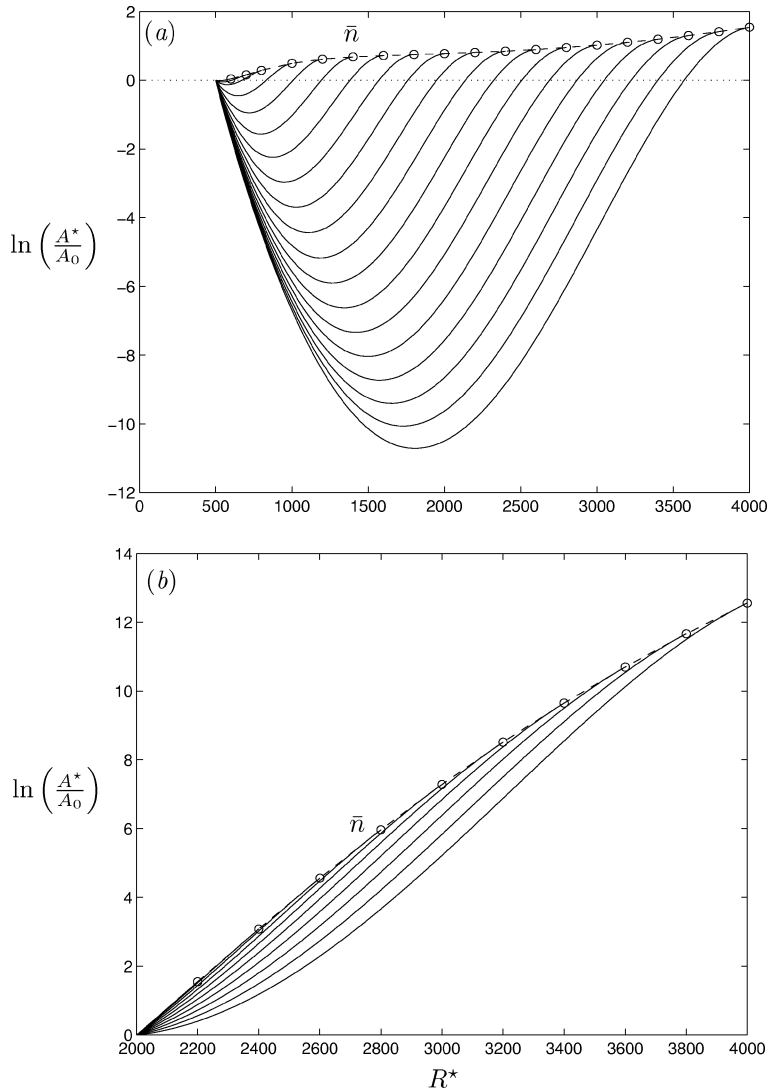

Figure 12. Maximum amplitudes $\bar{n}$ within wave packets generated by an impulsive source at (a) $R_0 = 500$ and (b) $R_0 = 2000$, calculated at discrete $R^\star$ marked by ∘ and fitted by – – –. Amplitude curves of the fixed frequency components reaching maximum amplitude are given by ——.

and there are many $f^\star$ that satisfy this, but it is the purely real value of $f^\star$ that gives the maximum growth between given R_n and $R^\star$. So, the maximum amplitude derived here from an asymptotic steepest-descent method is an n-factor of the usual form (i.e. the maximum amplitude at a given position $R^\star$, given by any frequency, compared with its amplitude at its own first neutral point) and with $f_i^\star = 0$ is given by

$$\max_f \left[\ln\left(\frac{A^\star}{A_n}\right)\right] = -\frac{2}{1.7208^2}\int_{R_n(f^\star)}^{R^\star} \alpha_i\left(R, f^\star\right) dR = n. \tag{47}$$

This maximum amplitude can be found without calculating the whole wave packet.

As above, for a given $f_i^\star$ (equal to zero for the n-factor), a Newton–Raphson iteration scheme is used to converge on to a value of $f_r^\star$ that satisfies (46), starting from an estimated f_r. So, changes to f_r to make

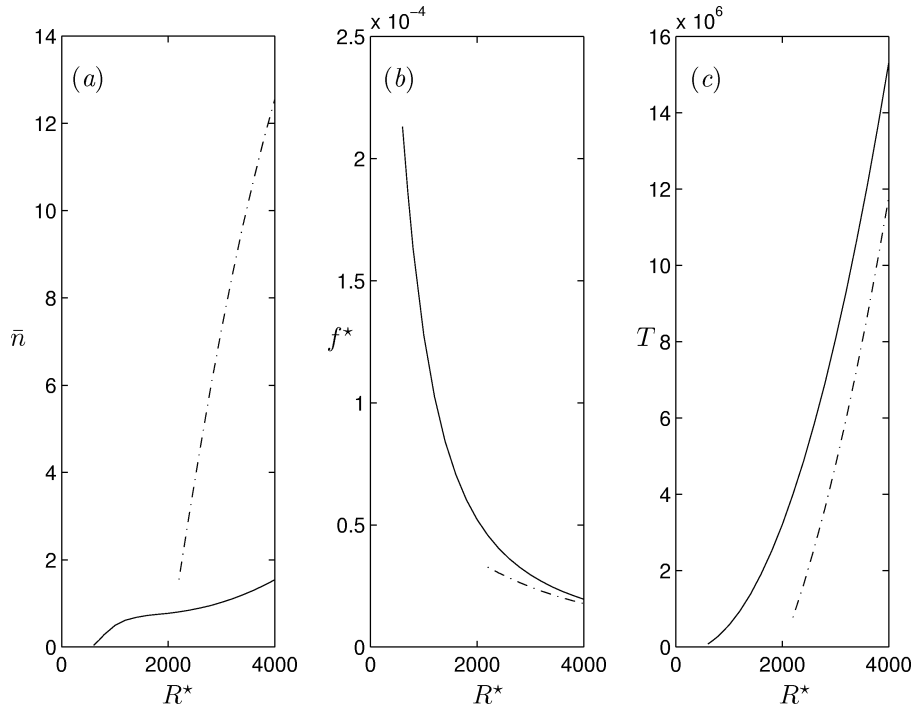

Figure 13. Variations in $\bar{n}$, $f^\star$ (real) and T with $R^\star$ for $R_0 = 500$ (——) and $R_0 = 2000$ (— · — ·).

$T_i \to 0$, are given by

$$\Delta f_r = -\frac{T_i}{J}, \tag{48}$$

where

$$J = \frac{\partial T_i}{\partial f_r} = \frac{2}{1.7208^2}\int_{R_0}^{R^\star} \frac{\partial^2 \alpha_i(R, f)}{\partial f_r^2}\, dR - \frac{\partial \overline{T_i}(f)}{\partial f_r}. \tag{49}$$

Figure 14 (solid lines) shows the amplitudes of some arbitrarily chosen frequencies normalized by the amplitudes at their own first neutral points. The usual e^n-approach would be to plot lots of these amplitude curves and then to fit an envelope curve that, at any given position, is tangent to the amplitude curve with largest value. This usual n-curve is indistinguishable from the dashed line in *figure 14* that is an interpolation of the discrete values of n ($\circ$) calculated using the asymptotic steepest-descent method described above with the starting positions, R_n, constrained to be neutral points, i.e. solutions of (47). *Figure 15* shows the magnitude of n and its projection on to the neutral curve (denoted by n_p) in the (f, R)-plane, where it lies close to the upper branch, and a selection of amplitude curves that form the n-factor. The variations in $f^\star$, R_n and T with $R^\star$ are shown in *figure 16*. The effects of non-zero $f_i^\star$ are given by *figures 17(a)* and *17(b)*. Here, the observation position is $R^\star = 2000$ and the starting position is $R_n = 1088$, i.e. the neutral point for the component reaching maximum amplitude at $R^\star = 2000$. Clearly, in *figure 17(a)*, the maximum amplitude is given by $f_i^\star = 0$, as expected; variations in $f_r^\star$ and T with $f_i^\star$ are also given. In *figure 17(b)* the wave packet envelope $(A^\star/A_n)$ is pictured against T for fixed $R^\star = 2000$. The leading and trailing edges are given by positive and negative $f_i^\star$, respectively.

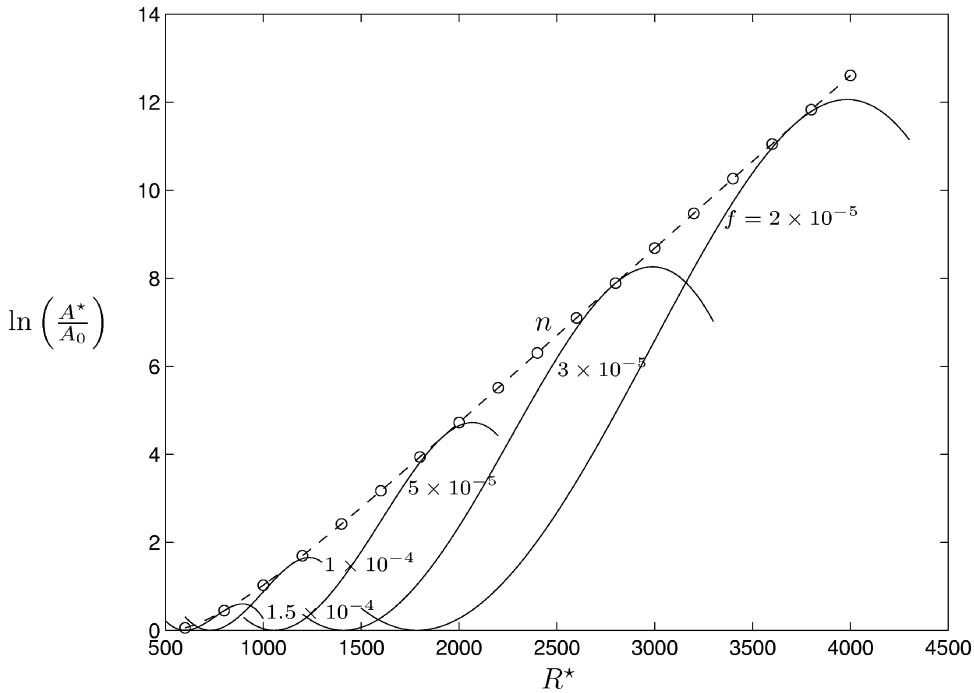

Figure 14. Amplitude curves for arbitrarily chosen frequencies normalized by the amplitudes at their own first neutral points (——) and the n-curve (– – –) calculated (not a fitted envelope) at discrete values of n (○).

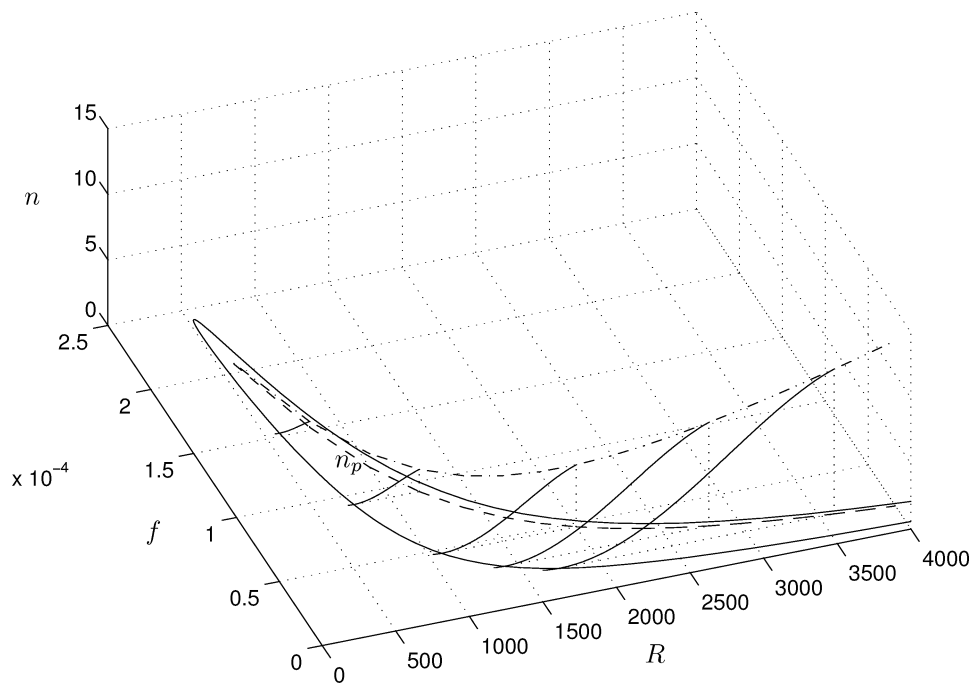

Figure 15. The magnitude of n (— · — ·) and its projection (denoted by n_p) (– – –) on to the neutral curve (——) in the (f, R)-plane, and a selection of amplitude curves (——) that form the n-factor.

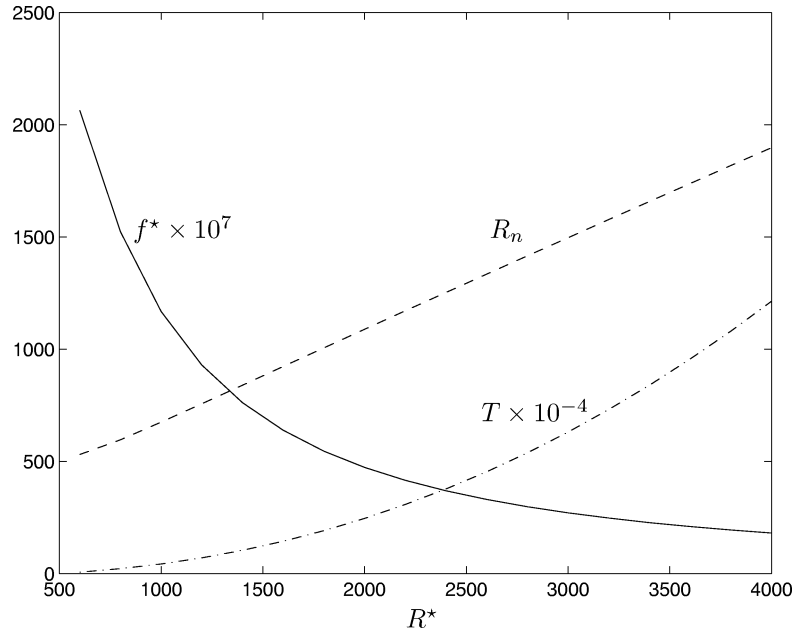

Figure 16. Variations in $f^\star$, R_n and T with $R^\star$.

3.2. Comments

A steepest-descent method applied to two-dimensional disturbances in a quasi-parallel two-dimensional boundary layer has been described. For this problem the usual approach to e^n-calculations, namely fitting an envelope curve to arbitrarily chosen real frequency curves, is straightforward and relatively fast. For these reasons it is not particularly recommended that the steepest-descent method be used for such boundary-layer flows. However, the discussion and examples given above illustrate the method for a case where the n-factor is undisputed and easily compared. For three-dimensional disturbances in three-dimensional quasi-parallel boundary layers there is significant dispute over approaches to e^n-calculations, and the added degree of freedom means that there is no consensus on how to find the maximum amplitude (worst case) at a given position in the boundary layer. In the following section the steepest-descent method is extended to cover three-dimensions, giving maximum amplitudes relevant to physical waves. The limitations are that, as yet, the mean flow is considered to be steady and independent of the spanwise direction. Examples of steady three-dimensional boundary-layer flows that satisfy these limitations are the rotating-disk boundary layer and the boundary layers on a cone at zero incidence and on infinite-span swept wings. It is the latter, i.e. the Falkner–Skan–Cooke similarity solution of the boundary-layer equations, that is considered in the following section.

3.3. Three-dimensional flows—the Falkner–Skan–Cooke boundary layer

The incompressible flow past an infinite swept wedge at zero angle of attack outside the viscous boundary layer is the Falkner–Skan–Cooke (FSC) potential flow (Cooke [28]). The flow can be represented in the chordwise direction (normal to the leading edge) by $U^*_{c\infty}$ and in the spanwise (parallel to the leading edge) direction by $V^*_{s\infty}$, where

$$U^*_{c\infty} = C^* \left(x^*_c\right)^m, \qquad V^*_{s\infty} = \text{constant}. \tag{50}$$

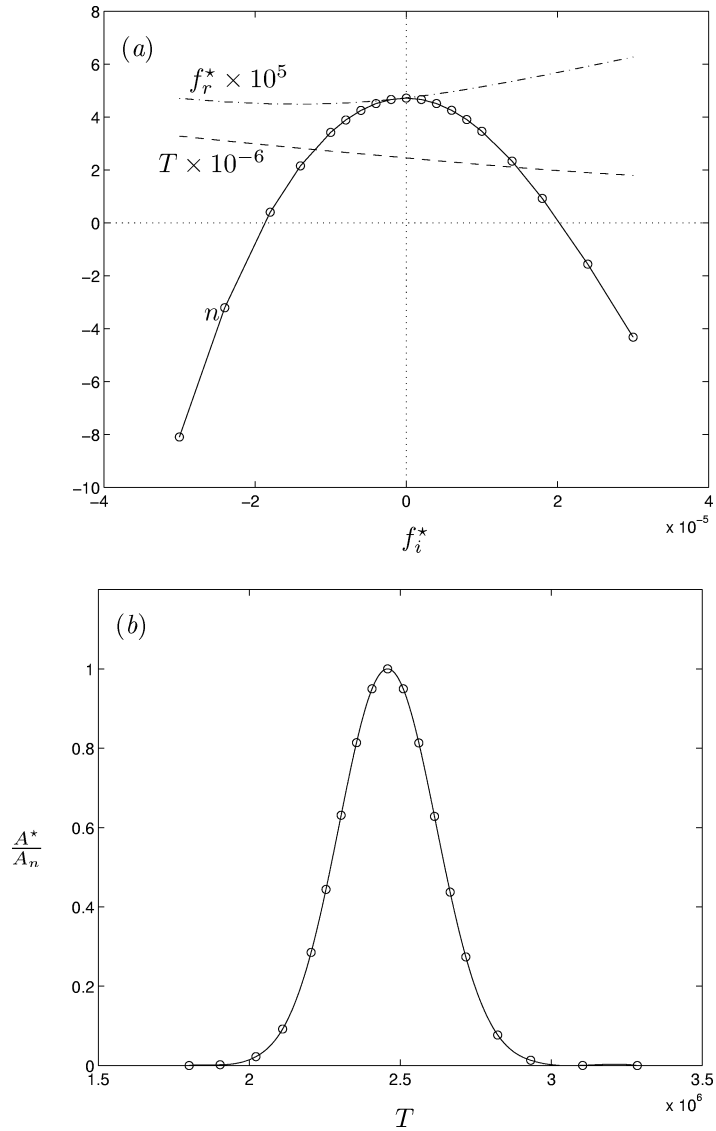

Figure 17. (a) The effects of non-zero $f_i^\star$ for $R^\star = 2000$ and $R_n = 1088$. (b) The wave packet envelope $(A^\star/A_n)$ against T for fixed $R^\star = 2000$.

As usual, the asterisks indicate dimensional quantities, the subscripts c and s indicate the chordwise and spanwise directions, respectively, x_c^* is the coordinate in the chordwise direction and C^* is a constant. The wedge angle is $\beta_H \pi/2$, where β_H is the usual two-dimensional (Falkner–Skan) pressure-gradient parameter, known as the Hartree parameter, and $\beta_H = 2m/(m+1)$. The similarity solution of the boundary-layer equations, in which the variables are functions of the wall-normal similarity variable $z = z^*/l^*$ only, where $l^* = [(m+1)U_{c\infty}^*/(2\nu^* x_c^*)]^{-1/2}$ and ν^* is the kinematic viscosity, is given (see Rosenhead [29]) by

$$f''' + ff'' + \beta_H\left(1 - f'^2\right) = 0, \tag{51}$$

$$g'' + fg' = 0, \tag{52}$$

where $f(z)' = U_c^*/U_{c\infty}^*$, $g(z) = V_s^*/V_{s\infty}^*$ and the primes indicate differentiation with respect to z. The boundary conditions are

$$f(0) = f'(0) = g(0) = 0, \qquad f'(\infty) = g(\infty) = 1. \tag{53}$$

The local potential flow is $U_\infty^* = (U_{c\infty}^{*2} + V_{s\infty}^{*2})^{1/2}$ and defines the streamwise direction, x, to which the cross-flow direction, y, is normal. The angle between the streamwise direction and the chordwise direction is the flow angle θ, where

$$\theta = \tan^{-1}\left(\frac{V_{s\infty}^*}{U_{c\infty}^*}\right). \tag{54}$$

Thus, there is no undisturbed freestream for FSC flows; the magnitude and direction of the freestream velocity vary with downstream position. The non-dimensional displacement thickness based on the streamwise velocity component is given by $\delta = \delta^*/l^*$. (For zero pressure gradient, i.e. $\beta_H = m = 0$, and any θ the flow reduces to the Blasius flow.) Physical quantities are non-dimensionalized using the length, time, velocity and pressure scales δ^*, δ^*/U_∞^*, U_∞^* and $\rho^* U_\infty^{*2}$, respectively. The Reynolds number based on the displacement thickness is then given by

$$R = \frac{\delta^* U_\infty^*}{\nu^*}, \tag{55}$$

and the chordwise Reynolds number based on x_c^* and $U_{c\infty}^*$ is

$$R_c = \frac{x_c^* U_{c\infty}^*}{\nu^*}. \tag{56}$$

The normal modes have the following form:

$$u(x_c, y_s, z, t) = A_0 \hat{u}(x_{c1}, z) e^{-i\Psi(x_c, y_s, z, t)X}, \tag{57}$$

where $X = x_c - x_{c0}$, $x_{c1} = \varepsilon x_c$ is the slow scale and

$$\Psi(x_c, y_s, z, t) = -\frac{1}{X}\left[\int_{x_{c0}}^{x_c} \alpha(x_{c1})\, dx_c + \beta(y_s - y_{s0}) - \omega t\right], \tag{58}$$

and α, β and ω are the chordwise wavenumber, spanwise wavenumber and frequency, respectively. As is usual with the quasi-parallel approach, A_0 is the initial amplitude and contributions to the amplitude are due only to the imaginary part of the phase function Ψ. The mean flow is given by the locally parallel FSC similarity solution and the eigenvalues α, β and ω satisfy a local dispersion relation (for the Orr–Sommerfeld equation and coupled Squire-mode equation; see Lingwood [16]). The eigenvalues at successive x_c-positions must be related such that they represent the propagation of a physical wave through the boundary layer, which for mean flows that are steady and independent of y_s implies that both the dimensional frequency and spanwise wavenumber are constant as a wave propagates.

Consider the response to a point impulsive forcing of the form

$$w(0; x_c, y_s, t) = \delta(X)\delta(Y)\delta(t), \tag{59}$$

where $Y = y_s - y_{s0}$, which is given by

$$w(z; x_c, y_s, t) = \frac{1}{(2\pi)^3}\int_W \int_B \int_A \frac{\Phi}{\Delta_0} e^{-i\Psi X}\, d\alpha\, d\beta\, d\omega, \tag{60}$$

where Φ is a function of z, and A, B and W are the inversion contours in the α-, β- and ω-planes, respectively. The α-inversion of (60) is performed first using the residue theorem leaving α as a function of β and ω, as well as x_c. Only residue contributions from poles corresponding to physical responses in the region $X > 0$ are considered. As $X \to \infty$ with t/X and Y/X constant, the asymptotic impulse response (at $x_c^{\star *}$ or, equivalently, $R_c^\star$) is dominated by contributions from the saddle points of Ψ, i.e. contributions from frequencies and spanwise wavenumbers that give stationary points of Ψ. In dimensional terms, this implies that

$$\int_{x_{c0}^*}^{x_c^{\star *}} \frac{\partial \alpha^*(x_c^*, \beta^{\star *}, \omega^{\star *})}{\partial \omega^*}\, dx_c^* = t^* \tag{61}$$

and

$$\int_{x_{c0}^*}^{x_c^{\star *}} \frac{\partial \alpha^*(x_c^*, \beta^{\star *}, \omega^{\star *})}{\partial \beta^*}\, dx_c^* = -Y^*, \tag{62}$$

where frequencies and spanwise wavenumbers that satisfy these relationship are denoted by a $\star$-superscript and are kept constant during the integrations over x_c^*. (The argument given in Section 3.1 can be extended to the three-dimensional case to show that the maximum-growth saddle point always contributes to the asymptotic impulse response.)

As with the Blasius boundary layer, it is usual to denote the dimensionless frequency by $f = \omega^* \nu^* / U_\infty^{*2}$, rather than ω, but here (due to U_∞^*) f is also a function of x_c for constant ω^*. The variable dimensionless frequency for constant ω^* is given by

$$f(R_c) = \left[\left(\frac{R_{c1}}{R_c} \right)^{2m/(m+1)} \frac{\cos^2 \theta}{\cos^2 \theta_1} \right] f(R_{c1}); \tag{63}$$

similarly the variable dimensionless spanwise wavenumber for constant β^* is

$$\beta(R_c) = \left[\left(\frac{R_{c1}}{R_c} \right)^{m/(m+1)} \frac{R \cos \theta}{R_1 \cos \theta_1} \right] \beta(R_{c1}), \tag{64}$$

where $f(R_c)$ and $\beta(R_c)$ are defined with respect to a reference point (1-subscript). The choice of reference conditions results in maximum amplitudes due only to the TS instability over the range of Reynolds numbers considered; the conditions are given in Appendix A. The varying freestream velocity complicates the non-dimensionalization of (61) and (62) to the extent that the functions τ and Υ in the following dimensionless equations derived from (61) and (62) are given in Appendix B (as is the dimensionless relationship between R_c and R). Both T and Y (the time a given wave takes to reach $R_c^\star$ from R_{c0} and the spanwise displacement when the wave reaches $R_c^\star$, respectively) must be real and, therefore, the imaginary part of the two integrals (61) and (62) must be zero:

$$\int_{R_{c0}}^{R_c^\star} \tau \frac{\partial \alpha_i(R_c, \beta^\star(R_c), f^\star(R_c))}{\partial f_r}\, dR_c = T_i = 0 \tag{65}$$

and

$$\int_{R_{c0}}^{R_c^\star} \Upsilon \frac{\partial \alpha_i(R_c, \beta^\star(R_c), f^\star(R_c))}{\partial \beta_r}\, dR_c = -Y_i = 0, \tag{66}$$

where $\beta^\star$ and $f^\star$ vary according to (64) and (63) so that dimensional values are held constant over the integration, and T and Y are non-dimensionalized using conditions at the observation position, i.e. $T = tR^\star = t^* U_\infty^{*2}/\nu^*$ and $Y = Y^*/\delta^*$, where U_∞^* and δ^*, respectively, are evaluated at the end observation position.

Although T_i and Y_i are zero at $R_c^\star$, the integrands of (65) and (66) are, in general non-zero for values of R_c between R_{c0} and $R_c^\star$, and T and Y are complex at all but the start and end positions.

The growth of a component of the wave packet is given by the imaginary part of the phase function

$$\begin{aligned}\Psi_i^\star X &= \ln\left(\frac{A^\star}{A_0}\right)\\ &= \ln\overline{U} + f_i^\star(R_c^\star)\int_{R_{c0}}^{R_c^\star}\tau\frac{\partial\alpha_r(R_c,\beta^\star(R_c),f^\star(R_c))}{\partial f_r}\,dR_c + \beta_i(R_c^\star)\int_{R_{c0}}^{R_c^\star}\Upsilon\frac{\partial\alpha_r(R_c,\beta^\star(R_c),f^\star(R_c))}{\partial\beta_r}\,dR_c\\ &\quad - \int_{R_{c0}}^{R_c^\star}\alpha_i\big(R_c,\beta^\star(R_c),f^\star(R_c)\big)\frac{R^{\star2}\Upsilon^2}{R^2\tau}\,dR_c\\ &= \ln\overline{U} + f_i^\star(R_c^\star)T - \beta_i(R_c^\star)Y - \int_{R_{c0}}^{R_c^\star}\alpha_i\big(R_c,\beta^\star(R_c),f^\star(R_c)\big)\frac{R^{\star2}\Upsilon^2}{R^2\tau}\,dR_c,\end{aligned}\tag{67}$$

where $\ln\overline{U}$ is due to the change in non-dimensionalizing velocity scale between R_{c0} and $R_c^\star$, and is defined in Appendix B. As in Section 3.1, the growth can be maximized with respect to T and also with respect to Y to find the component arriving at $R_c^\star$ with the largest amplitude compared with its amplitude at R_{c0}. It is found that $\beta_i^\star(R_c) = f_i^\star(R_c) = 0$ gives the maximum growth

$$\Psi_{i\max}^\star X = \max_{\beta,f}\left[\ln\left(\frac{A^\star}{A_0}\right)\right] = -\int_{R_{c0}}^{R_c^\star}\alpha_i\big(R_c,\beta^\star(R_c),f^\star(R_c)\big)\frac{R^{\star2}\Upsilon^2}{R^2\tau}\,dR_c = \bar{n}.\tag{68}$$

As with the two-dimensional example in the previous section, $\bar{n}$ is highly dependent on R_{c0} and, if these amplitudes are to be used for transition prediction, it is necessary to find the value of R_{c0} that results in the largest amplitude at a given $R_c^\star$, i.e. to find the worst case. By extension of the two-dimensional case, it can be shown that $\Psi_{i\max}^\star X$ has a maximum over all R_{c0} when R_{c0} is a neutral point. Let $\Psi_{i\max}^\star X = \psi^\star(R_{c0},\beta^\star(R_c),f^\star(R_c);R_c^\star)$, where $\beta_i^\star(R_c) = f_i^\star(R_c) = 0$ for maximum growth over T and Y at $R_c^\star$, then when

$$\frac{d(\Psi_{i\max}^\star X)}{dR_{c0}} = \frac{\partial\psi^\star}{\partial f_r(R_c^\star)}\frac{df_r(R_c^\star)}{dR_{c0}} + \frac{\partial\psi^\star}{\partial\beta_r(R_c^\star)}\frac{d\beta_r(R_c^\star)}{dR_{c0}} + \frac{\partial\psi^\star}{\partial R_{c0}} = 0,\tag{69}$$

$\partial\psi^\star/\partial R_{c0} = -\alpha_i(R_{c0},\beta^\star(R_{c0}),f^\star(R_{c0})) = 0$ because in the first two terms on the right-hand side of (69) $\partial\psi^\star/\partial f_r(R_c^\star) = -T_i$ and $\partial\psi^\star/\partial\beta_r(R_c^\star) = Y_i$, which are zero for $f^\star$ and $\beta^\star$. Thus, for a given $R_c^\star$, α is purely real at R_{c0}, i.e. R_{c0} is a neutral point because both $\beta^\star$ and $f^\star$ are also real.

As in Section 3.1, allowing the neutral point (a function of frequency and spanwise wavenumber) to be denoted by $R_{cn}(\beta,f)$ and R_{c0} now to be a position farther upstream in the stable region, then the time taken for a disturbance to travel from R_{cn} to the chosen $R_c^\star$ and the spanwise displacement of that component can be written, in dimensionless terms, as

$$\begin{aligned}T &= \int_{R_{c0}}^{R_c^\star}\tau\frac{\partial\alpha(R_c,\beta^\star(R_c),f^\star(R_c))}{\partial f}\,dR_c - \int_{R_{c0}}^{R_{cn}(\beta^\star,f^\star)}\tau\frac{\partial\alpha(R_c,\beta^\star(R_c),f^\star(R_c))}{\partial f}\,dR_c\\ &= \int_{R_{c0}}^{R_c^\star}\tau\frac{\partial\alpha(R_c,\beta^\star(R_c),f^\star(R_c))}{\partial f}\,dR_c - \overline{T}(\beta^\star,f^\star),\end{aligned}\tag{70}$$

$$\begin{aligned}Y &= -\int_{R_{c0}}^{R_c^\star}\Upsilon\frac{\partial\alpha(R_c,\beta^\star(R_c),f^\star(R_c))}{\partial\beta}\,dR_c + \int_{R_{c0}}^{R_{cn}(\beta^\star,f^\star)}\Upsilon\frac{\partial\alpha(R_c,\beta^\star(R_c),f^\star(R_c))}{\partial\beta}\,dR_c\\ &= -\int_{R_{c0}}^{R_c^\star}\Upsilon\frac{\partial\alpha(R_c,\beta^\star(R_c),f^\star(R_c))}{\partial\beta}\,dR_c - \overline{Y}(\beta^\star,f^\star),\end{aligned}\tag{71}$$

where the two terms that form T and Y are individually complex, but where (for $\beta^\star$ and $f^\star$) T and Y are themselves real, and where the integration limits of the first of the right-hand-side terms are independent of spanwise wavenumber and frequency. Hence, if T and Y are to be real, then the saddle-point conditions become

$$T_i = \int_{R_{c0}}^{R_c^\star} \tau \frac{\partial \alpha_i(R_c, \beta^\star(R_c), f^\star(R_c))}{\partial f_r}\, dR_c - \overline{T_i}(\beta^\star, f^\star) = 0, \tag{72}$$

$$Y_i = -\int_{R_{c0}}^{R_c^\star} \Upsilon \frac{\partial \alpha_i(R_c, \beta^\star(R_c), f^\star(R_c))}{\partial \beta_r}\, dR_c - \overline{Y_i}(\beta^\star, f^\star) = 0. \tag{73}$$

Again, it is the purely real values of $f^\star$ and $\beta^\star$ that give the maximum growth between given R_{cn} and $R_c^\star$. So, the maximum amplitude is an n-factor that is analogous in form to the usual two-dimensional n-factor, i.e. the maximum amplitude at a given position $R_c^\star$ of any disturbance compared with its amplitude at its own the first neutral point, but here derived from an asymptotic steepest-descent method

$$\max_{\beta, f}\left[\ln\left(\frac{A^\star}{A_n}\right)\right] = -\int_{R_{cn}(\beta^\star, f^\star)}^{R_c^\star} \alpha_i\big(R_c, \beta^\star(R_c), f^\star(R_c)\big) \frac{R^{\star 2}\Upsilon^2}{R^2\tau}\, dR_c = n. \tag{74}$$

This maximum amplitude can be found without calculating the whole wave packet.

For given $\beta_i^\star$ and $f_i^\star$ (equal to zero for the n-factor), a two-dimensional Newton–Raphson iteration scheme is used to converge on to values of $\beta_r^\star$ and $f_r^\star$ that satisfy (72) and (73), starting from estimates of β_r and f_r. So, changes to β_r and f_r that make $T_i \to 0$ and $Y_i \to 0$, are given by

$$\begin{pmatrix} \Delta f_r(R_{c0}) \\ \Delta \beta_r(R_{c0}) \end{pmatrix} = -\begin{pmatrix} J_{11} & J_{12} \\ J_{21} & J_{22} \end{pmatrix}^{-1} \begin{pmatrix} T_i \\ Y_i \end{pmatrix}, \tag{75}$$

where the components of matrix **J** are given in Appendix B.

Figure 18 shows the n-curve, interpolated between the discrete values of n ($\circ$), calculated using the steepest-descent method described above, where the starting positions, R_{cn}, are constrained to be neutral points, i.e. solutions of (74). The variations in $\beta^\star(R_{cn})$, $f^\star(R_{cn})$, R_{cn}, Y and T with $R_c^\star$ are shown in *figure 19*. The effects of non-zero $\beta_i^\star(R_{c1})$ and $f_i^\star(R_{c1})$ are given by *figures 20(a)* and *20(b)*. Here, the observation position is $R_c^\star = 5 \times 10^5$ and the initiation position is $R_{cn} = 1.7890 \times 10^5$, i.e. the neutral point for the component reaching maximum amplitude at the given $R_c^\star$. Clearly, in *figure 20(a)*, the maximum amplitude is given by $\beta_i^\star = f_i^\star = 0$, as expected; variations in T, Y, $f_r^\star(R_{c1})$ and $\beta_r^\star(R_{c1})$ with $\beta_i^\star$ and $f_i^\star$ are also given. (Convergence problems were encountered for $f_i^\star < -2.3 \times 10^{-5}$.) In *figure 20(b)* the wave packet envelope ($A^\star/A_n$) is pictured against Y and T for fixed $R_c^\star = 5 \times 10^5$. Just the two paths where $\beta_i^\star = 0$ and $f_i^\star = 0$ are shown, giving an indication of the surface of the wave-packet envelope. The projections of the two paths on to the (T, Y)-plane are also given. The remainder of the surface is given by $\beta^\star$ and $f^\star$ both with non-zero imaginary parts.

3.4. Comparison of three-dimensional e^n-methods

As a reminder, the question of whether the e^n-method alone is useful for laminar–turbulent transition prediction, and the value of n that compares well with the experimentally observed onset of transition, are not the concern of this paper; here the concern is how to calculate physically relevant amplitudes in growing three-dimensional boundary layers. Existing three-dimensional e^n-methods lead to different n-factors for the same basic flow, which is clearly unsatisfactory. Here it is suggested that the spatial steepest-descent method (valid for large X) leads to physically relevant disturbance amplitudes, at least to within the approximations of linearity,

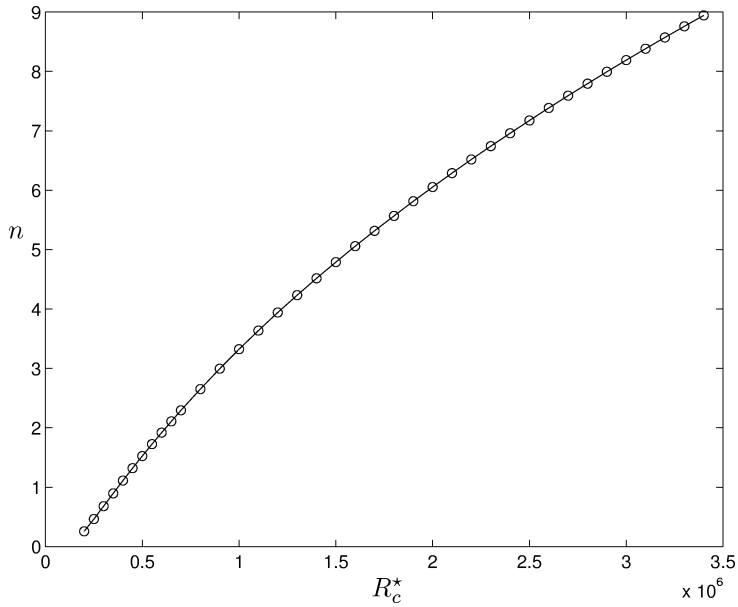

Figure 18. The n-curve (– – –) calculated at discrete values of n (∘).

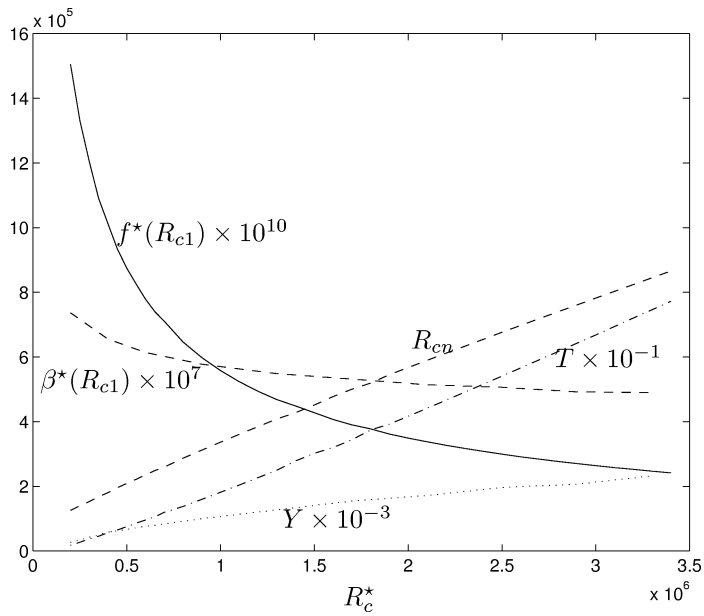

Figure 19. Variations in $\beta^\star(R_{cn})$, $f^\star(R_{cn})$, R_{cn}, Y and T with $R_c^\star$.

the neglect of receptivity, absolute instability and bypass mechanisms and of the quasi-parallel approach (all approximations that the existing e^n-methods also make). Comparison with experiments would be needed to check that laminar–turbulent transition does not occur within the transient regime before the asymptotic method becomes valid. In this section, for simplicity of notation, β and ω will be used for the spanwise wavenumber and frequency, respectively, with the assumption that they are proportional to constant values of the respective dimensional quantities; this is only true if the non-dimensionalizing scales are independent of x.

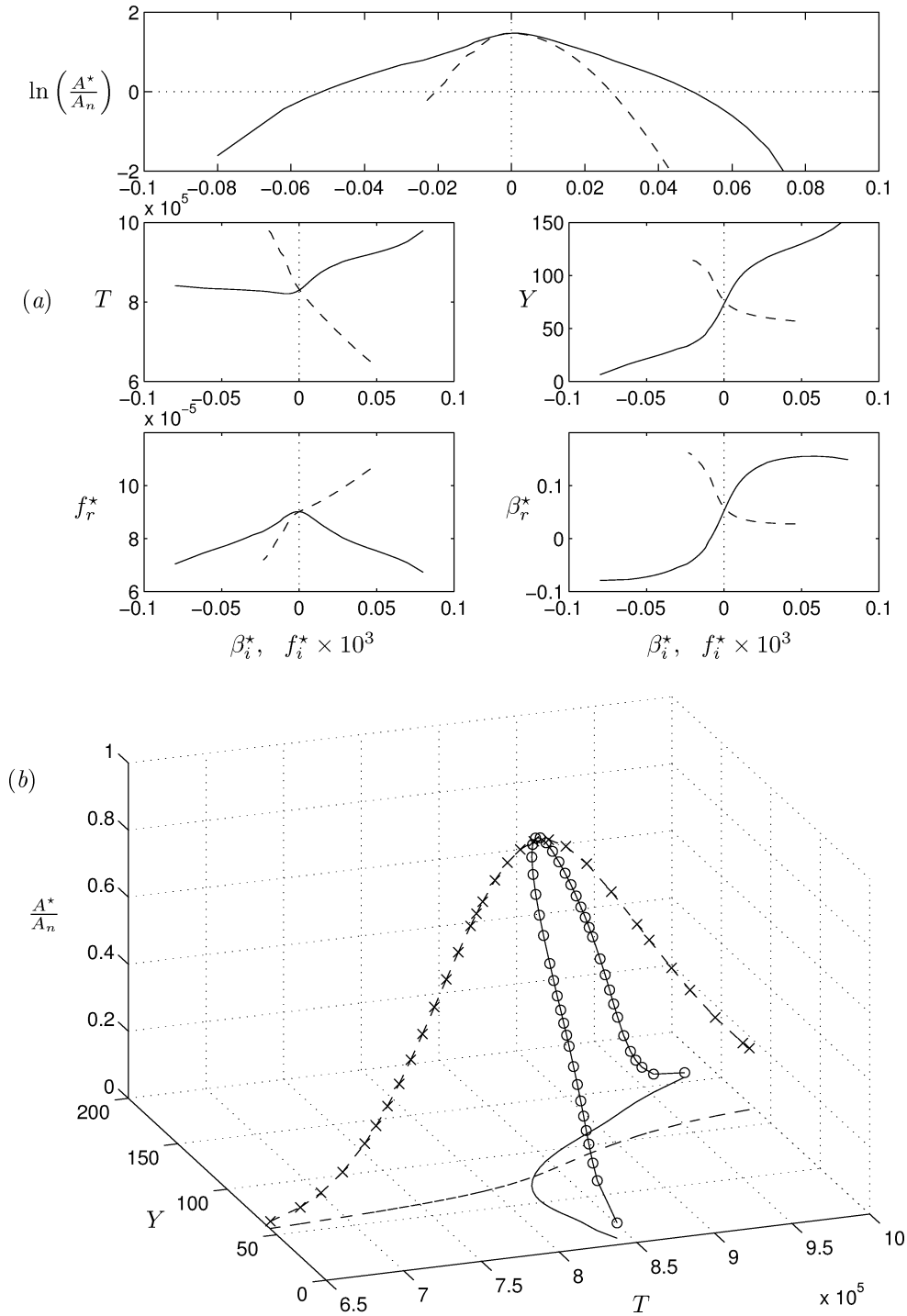

Figure 20. (a) The effects of non-zero $\beta_i^\star$ with $f_i^\star = 0$ (——) and non-zero $f_i^\star$ with $\beta_i^\star = 0$ (– – –) for $R_c^\star = 5 \times 10^5$ and $R_{cn} = 1.7690 \times 10^5$. (b) Part of the wave packet envelope $(A^\star/A_n)$ against Y and T for fixed $R_c^\star = 5 \times 10^5$ given by $f_i^\star = 0$ ((∘) and (——) when projected on to the $[T, Y]$-plane) and $\beta_i^\star = 0$ ((×) and (– – –) when projected on to the $[T, Y]$-plane).

The most popular three-dimensional e^n-method is the envelope method. The method is as follows. For a fixed frequency wave at a fixed Reynolds number the wave angle ($\varepsilon = \tan^{-1}(\beta_r/\alpha_r)$) is optimized to find the wave angle that gives the maximum spatial growth rate. This procedure is repeated at successive downstream positions (or Reynolds numbers) so that the successive maximized growth rates are effectively given by a function of the optimized wave angle and Reynolds number. Thus, for each harmonic forcing,

$$\ln\left(\frac{A}{A_0}\right) = \int_{x_0}^{x} \max_{\varepsilon}\left[\sigma(x)\right] dx, \tag{76}$$

where σ is used to denote the x-dependent spatial growth rate that could be defined in a number ways: the temporal growth rate ω_i converted to a spatial growth rate via an assumed real group velocity factor, or simply $-\alpha_i$ if β_i is assumed to be zero, or $-\alpha_i - \beta_i y/x$ where the value of β_i is decided using some extra condition and y/x is constant; see the discussion of the Cebeci–Stewartson method below. The n-factor is then (76) maximized over all real frequencies. Even if the ambiguity of the definition of σ is ignored for a moment, the concept is flawed because piecing together successive maximum growth rates does not represent the growth of a physical disturbance, but rather represents jumping successively between waves with different β_r, which is unphysical for boundary layers that are independent of the spanwise coordinate; what is required is the maximum *integrated* growth of a physical wave at some observation position x (as with the steepest-descent method proposed here) not a string of maximum growth *rates*. The envelope method takes no account of separate instability modes (such as TS and crossflow modes) and results in a single n-curve with magnitude larger than any physical wave ever reaches at a given x-position. In fact, as the dominance of the modes changes with changing Reynolds number, $\max_\varepsilon[\sigma]$ will jump from relating to one type of instability mode to the other, possibly leading to a large abrupt change in ε.

Similarly the method proposed by Brevdo [21], and discussed in Section 2.7, consists of piecing together successive maximum spatial growth rates (and integrating along a path defined by the directions of propagation of these successive maximum growth rates) from analysis of successive assumed locally-parallel regions of the flow. These maximum spatial growth rates are shown in Section 2 to be given by successive maxima in sheets of spatial dispersion relation $-\alpha_{im} \equiv \max[-\alpha_i(\beta_r, \omega_r)]$ (see (28)), where β and ω are purely real. If the boundary layer really is parallel, e.g. the Ekman layer, then $-\alpha_{im}$ is easily found and correctly gives the maximum growth rate, which applies at all positions. Admittedly, Brevdo's method for non-parallel three-dimensional boundary layers of piecing together successive $-\alpha_{im}$ has the advantage that these growth rates are still easy to find, and the method would be relatively fast because the growth rate is maximized over both β and ω before integrating, whereas with the envelope method the procedure is repeated for all real ω and the maximization over frequency is done after integrating. However, at least the envelope method considers waves of fixed frequency, even if the spanwise wavenumber is allowed to vary unphysically. Further, it is difficult to see how the concept of normalizing by the amplitude at the neutral point can be incorporated into Brevdo's method when the frequency is not held constant.

Alternative methods have been used in an attempt to overcome the recognized unphysical disturbance evolutions required by the envelope method. These alternatives usually allow for separate e^n-calculations for separate instability modes and involve keeping two quantities constant as the integration of the growth rate proceeds downstream. This is repeated for all combinations of the two chosen quantities and then the integrated growth rates are maximized with respect to the two quantities. These methods are called envelope-of-envelope methods by Arnal [1]. One of the two quantities is always the frequency, and this is physically correct because waves maintain constant dimensional frequency in steady flows. The second quantity is either the total wavelength, the wave angle or the spanwise wavenumber. If the boundary-layer flow is independent of the spanwise coordinate it is easy to show that the dimensional β is independent of x, i.e. constant but not

necessarily real. Constant β implies that neither the total wavelength nor the wave angle of a physical wave is constant with changing x. So, it seems that the only envelope-of-envelope method that is likely to be correct is that proposed by Mack [5], which calculates and integrates successive spatial growth rates for waves with fixed ω and β (followed by maximization over all ω and β). The problem with this method is that, in general, there is no reason to consider only constant real spanwise wavenumbers (unless the forcing really is periodic in y), as Mack [5] did for an FSC boundary layer. Assuming a priori that $\beta_i = 0$ means that only growth in the x-direction is considered, which seems unsatisfactory. However, the spatial steepest-descent proposed in this paper shows that between any two points in the boundary layer, although both ω and β are complex in general, the maximum amplitude is given by a wave component with both real ω and β. So, maximization over all real frequency and spanwise wavenumber of Mack's integrated spatial growth rates, which (at a given x) are given simply by $-\alpha_i(\beta_r, \omega_r)$, will eventually lead to the same maximum amplitude as predicted by the steepest-descent method but the method is extremely labour intensive and, unlike the steepest-descent method, the spanwise location of that maximum amplitude component cannot be derived from Mack's method; the same amplitude is seen at all y for a fixed x.

Cebeci and Stewartson [6] suggested a method that provides an extra condition that removes the arbitrariness of the spanwise wavenumber. Their approach is discussed briefly in Section 1 and more fully in Section 2.4.1. It is also based on a spatial steepest-descent method, but considers harmonic forcing, i.e. ω is real and prescribed, and the phase function is of the form $\alpha + \beta y/x$. For each real frequency and x-position, this leads to a saddle-point condition given by

$$\frac{\partial \alpha}{\partial \beta} = -\frac{y}{x}, \tag{77}$$

which applies along rays of constant y/x and where the imaginary part of the partial derivative must be zero because y/x is real. The extra condition that $\partial \alpha_i / \partial \beta_r = 0$ fixes α and β (both complex in general, giving growth in both the x- and y-directions) for each value of y/x and ω. Then it is necessary to decide how to connect the values of α and β for fixed frequency given by different values of y/x at successive x-positions. Cebeci and Stewartson [6] originally suggested that values of y/x giving the maximum growth rate at each x-position should be selected, but they went on to say that this approach would be too complicated and, therefore, suggested that the value of y/x giving the maximum growth rate at each x-position be approximated by a constant value defined at the initial x-position. (Finally, the integrated growth rates are maximized over all real frequencies.) However, whichever route is taken, the implication is that β varies with x, which is unphysical for the three-dimensional boundary layers being considered. Furthermore, the steepest-descent method is only valid for large x and yet with the Cebeci–Stewartson method it is applied successively at neighbouring x-positions, i.e. it is assumed to apply successively at x-positions close to zero.

The multitude of conflicting approaches for three-dimensional boundary layers, none of which are equivalent to that proposed here, means that comparison with existing methods will not give agreement. Nevertheless, the method has been shown to give perfect agreement with the two-dimensional example in Section 3, for which the standard approach is accepted, and arguments are given above for why this method should give more physical results than existing methods for three-dimensional flows. Of course, experimental verification should follow.

4. Conclusions

In the first part of this paper it is shown that the maximum temporal or maximum spatial growth rate is easily found from maxima in either temporal or spatial sheets of the dispersion relation. This is illustrated using the Ekman layer, which is three-dimensional and strictly parallel. It is then argued that, despite existing

three-dimensional e^n-methods, piecing together such maximum growth rates (and directions of maximum growth rates) at successive locations in a two- or three-dimensional boundary layer does not correspond to the propagation and growth of a physical disturbance within a growing boundary layer. Here, all waves are excited simultaneously and a spatial steepest-descent method applicable to steady two- and three-dimensional boundary layers with slow spatial inhomogeneity in one direction is used to solve for the impulse response. The method is first illustrated using the Blasius boundary layer and then using a Falkner–Skan–Cooke boundary layer. Between the initiation and observation positions $\partial\alpha/\partial f$ and $\partial\alpha/\partial\beta$ are not constrained to be real, as suggested (at least in part) with steepest-descent analyses elsewhere; see Cebeci and Stewartson [6], Nayfeh [7] and Gaster [20]. Instead, the integrals of these quantities between the two positions in the boundary layer (with suitable non-dimensionalization scalings) are constrained to be real, because these integrals represent the time of travel and spanwise distance of travel of a disturbance, respectively. Thus, the method requires that, for x-positions between the initiation and observation positions, time and spanwise distance are extended into the complex plane, with the constraint that both are real at the downstream observation position. This constraint provides the extra condition necessary to remove the arbitrariness of the value of the spanwise wavenumber, which is the usual problem with spatial three-dimensional e^n-calculations where, with both α and β being in general complex, there are too many unknowns. The method has the considerable advantage that the whole wave packet does not need to be calculated; by restricting the solution set to real frequency and spanwise wavenumber only the maximum amplitude components are calculated as the observation position varies. The maximum amplitude components (and all other components if the whole wave packet is calculated) correspond to physical disturbances, namely both dimensional frequency and spanwise wavenumber are constant throughout the downstream propagation.

The initial position of the disturbance can either be a fixed point for all downstream observation points, in which case the solution is the true impulse response that is dependent on the initial position of the impulsive disturbance; given by (42) and (68) for the two- and three-dimensional cases, respectively. Alternatively, the initial position can be constrained to be always the neutral point on the lower branch of the neutral stability curve for the wave component under consideration; see (47) and (74) for the two- and three-dimensional cases, respectively. It is shown that, for both the two- and three-dimensional cases, the latter choice leads to the worst case (the largest possible amplitude for any initial disturbance position) at a given downstream observation position. Furthermore, in the two-dimensional case, it leads to the usual definition of the n-factor and application of the method to the Blasius boundary layer in this paper shows that the n-factor derived from the steepest-descent method is indistinguishable from that derived from fitting an envelope to growth curves for arbitrarily chosen harmonic waves. A three-dimensional n-factor can be derived that is analogous to the standard two-dimensional n-factor (i.e. the maximum amplitude at a given observation position reached by any wave starting at its own neutral point) and is justified because the resulting n-factor corresponds to the largest possible amplitude at the observation position.

The preceding section compares the method proposed here with existing methods. It is shown that the existing methods calculate the growth of unphysical waves and involve far more calculation than necessary, with maximization of amplitude coming at the end of all the calculations, rather than the analysis associated with the method proposed here that enables the solution set to be restricted to only the maximum amplitude components.

The method could be extended to account for flows that are dependent on the spanwise coordinate and it is not necessary to have the mean flow described by a similarity solution; the mean flow could just as well be derived from a more general solution of the boundary-layer equations. Furthermore, the method could be used to find the separate maximum amplitudes due to separate instability modes, such as Tollmien–Schlichting and crossflow modes, and give individual n-factors. (For the FSC example given in this paper only the TS mode is

considered.) This would rely on the instability modes being sufficiently well separated in the parameter space, but this is usually the case.

Appendix A. Reference conditions

The reference conditions have not been chosen for any particular reason, but are

$$\begin{aligned} \beta_H &= 0.01, & R_{c1} &\approx 81244, \\ \theta_1 &= 15^\circ, & \delta_1 &\approx 1.2011, \\ x^*_{c1} &= 0.1\ \text{m}, & U^*_{c\infty 1} &\approx 11.780\ \text{m s}^{-1}, \\ \nu^* &= 1.45 \times 10^{-5}\ \text{m}^{-2}\,\text{s}, & l^*_1 &\approx 4.9491 \times 10^{-4}\ \text{m}, \\ R_1 &= 500, & V^*_{s\infty} &\approx 3.1566\ \text{m s}^{-1}. \end{aligned}$$

Appendix B. Functions

The functions from Section 3.3 are

$$\frac{R}{R_1} = \frac{\delta}{\delta_1}\left[\frac{R_c(1+\tan^2\theta)}{R_{c1}(1+\tan^2\theta_1)}\right]^{1/2}, \tag{78}$$

$$\tau = \left(\frac{R^\star_c}{R_c}\right)^{2m/(m+1)} \frac{\cos\theta}{R(m+1)\cos^2\theta^\star}, \tag{79}$$

$$\Upsilon = \left(\frac{R^\star_c}{R_c}\right)^{m/(m+1)} \frac{1}{R^\star(m+1)\cos\theta^\star}, \tag{80}$$

$$\overline{U} = \frac{U^{\star *}_\infty}{U^*_{\infty 0}} = \left(\frac{R^\star_c}{R_{c0}}\right)^{m/(m+1)} \frac{\cos\theta_0}{\cos\theta^*}, \tag{81}$$

where throughout 0- and 1-subscripts denote that the quantity is evaluated at R_{c0} and R_{c1} (the reference position), respectively, and $\star$-superscripts denote evaluation at $R^\star_c$.

The components of matrix **J** in (75) are

$$\begin{aligned} J_{11} &= \frac{\partial t_i}{\partial f_r(R_{c0})} = \int_{R_{c0}}^{R^\star_c} \tau\mathcal{F}\frac{\partial^2\alpha_i(R_c,\beta(R_c),f(R_c))}{\partial f_r^2}\,dR_c - \frac{\partial \bar{t}_i}{\partial f_r(R_{c0})}, \\ J_{12} &= \frac{\partial t_i}{\partial \beta_r(R_{c0})} = \int_{R_{c0}}^{R^\star_c} \tau\mathcal{B}\frac{\partial^2\alpha_i(R_c,\beta(R_c),f(R_c))}{\partial \beta_r \partial f_r}\,dR_c - \frac{\partial \bar{t}_i}{\partial \beta_r(R_{c0})}, \\ J_{21} &= \frac{\partial Y_i}{\partial f_r(R_{c0})} = -\int_{R_{c0}}^{R^\star_c} \Upsilon\mathcal{F}\frac{\partial^2\alpha_i(R_c,\beta(R_c),f(R_c))}{\partial f_r \partial \beta_r}\,dR_c - \frac{\partial \overline{Y}_i}{\partial f_r(R_{c0})}, \\ J_{22} &= \frac{\partial Y_i}{\partial \beta_r(R_{c0})} = -\int_{R_{c0}}^{R^\star_c} \Upsilon\mathcal{B}\frac{\partial^2\alpha_i(R_c,\beta(R_c),f(R_c))}{\partial \beta_r^2}\,dR_c - \frac{\partial \overline{Y}_i}{\partial \beta_r(R_{c0})}, \end{aligned} \tag{82}$$

where

$$\mathcal{F} = \left(\frac{R_{c0}}{R_c}\right)^{2m/(m+1)} \frac{\cos^2\theta}{\cos^2\theta_0} \tag{83}$$

and

$$\mathcal{B} = \left(\frac{R_{c0}}{R_c}\right)^{m/(m+1)} \frac{R\cos\theta}{R_0\cos\theta_0}, \tag{84}$$

which are the scalings of $f(R_c)$ and $\beta(R_c)$ with respect to their values at R_{c0} for constant dimensional frequency and spanwise wavenumber; see (63) and (64) where $f(R_c)$ and $\beta(R_c)$ are compared with their values at the reference point.

Acknowledgements

This work was supported by a Research Fellowship at Pembroke College, Cambridge, and has benefited from discussions with Dr. S.J. Cowley.

References

[1] Arnal D., Boundary layer transition: predictions based on linear theory, in: AGARD-VK1 Special Course on Progress in Transition Modelling, 1993, pp. 2.1–2.63.
[2] Smith A.M.O., Gamberoni N., Transition, pressure gradient and stability theory, Douglas Aircraft Co. Report, ES 26388, CA, 1956.
[3] Van Ingen J.L., A suggested semi-empirical method for the calculation of the boundary layer transition region, Aero. Eng. Department Report, UTH-74, Technical University, Delft, 1956.
[4] Gaster M., A note on the relation between temporally increasing and spatially increasing disturbances in hydrodynamic stability, J. Fluid Mech. 14 (1962) 222–225.
[5] Mack L.M., Stability of three-dimensional boundary layers on swept wings at transonic speeds, in: Zierep J., Oertel H. (Eds), Proc. IUTAM Symposium Transsonicum III, Springer, 1988.
[6] Cebeci T., Stewartson K., On stability and transition in three-dimensional flows, AIAA J. 18 (1980) 398–405.
[7] Nayfeh A.H., Stability of three-dimensional boundary layers, AIAA J. 18 (1979) 406–416.
[8] Huerre P., Monkewitz P.A., Local and global instabilities in spatially developing flows, Ann. Rev. Fluid Mech. 22 (1990) 473–537.
[9] Lingwood R.J., An experimental study of absolute instability of the rotating-disk boundary-layer flow, J. Fluid Mech. 314 (1996) 373–405.
[10] Briggs R.J., Electron-Stream Interaction with Plasmas, MIT Press, 1964, chap. 2.
[11] Bers A., Linear waves and instabilities, in: DeWitt C., Peyraud J. (Eds), Physique des Plasmas, Gordon and Breach, 1975, pp. 117–215.
[12] Lingwood R.J., Absolute instability of the boundary layer on a rotating disk, J. Fluid Mech. 299 (1995) 17–33.
[13] Lingwood R.J., Absolute instability of the Ekman layer and related rotating flows, J. Fluid Mech. 331 (1997) 405–428.
[14] Lingwood R.J., On the effects of suction and injection on the absolute instability of the rotating-disk boundary layer, Phys. Fluids 9 (1997) 1317–1328.
[15] Lingwood R.J., On the application of the Briggs' and steepest-descent methods to a boundary-layer flow, Stud. Appl. Math. 98 (1997) 213–254.
[16] Lingwood R.J., On the impulse response for swept boundary-layer flows, J. Fluid Mech. 344 (1997) 317–334.
[17] Ekman V.W., On the influence of the earth's rotation on ocean currents, Ark. Mat. Astr. Fys. 2 (11) (1905).
[18] Gaster M., Growth of disturbances in both space and time, Phys. Fluids 11 (1968) 723–727.
[19] Von Kármán T., Über laminare und turbulente Reibung, Z. Angew. Math. Mech. 1 (1921) 233–252.
[20] Gaster M., Estimates of errors incurred in various asymptotic representations of wave packets, J. Fluid Mech. 121 (1982) 365–377.
[21] Brevdo L., Absolute and convective instabilities and the e^n method for prediction of the laminar–turbulent transition, ZAMM 74 (1994) 340–343.
[22] Gaster M., Propagation of linear wave packets in laminar boundary layers, AIAA J. 19 (1981) 419–423.
[23] Spooner G.F., Criminale W.O., The evolution of disturbances in an Ekman boundary layer, J. Fluid Mech. 115 (1982) 327–346.
[24] Brevdo L., Three-dimensional absolute and convective instabilities and spatially amplifying waves in parallel shear flows, ZAMP 42 (1991) 911–942.
[25] Taylor M.J., Peake N., The long-time behaviour of incompressible swept-wing boundary layers subject to impulsive forcing, J. Fluid Mech. 355 (1998) 359–381.
[26] Taylor M.J., Peake N., The long-time impulse response of compressible swept wing boundary layers, J. Fluid Mech. 379 (1999) 333–350.
[27] Mack L.M., Special course on stability and transition of laminar flow, AGARD Report 709, NATO, 1984.
[28] Cooke J.C., The boundary layer of a class of infinite yawed cylinders, Proc. Cambridge Philos. Soc. 46 (1950) 645–648.
[29] Rosenhead L., Laminar Boundary Layers, OUP, 1963, pp. 470–471.